

Stochastic Adaptive Estimation in Polynomial Curvature Shape State Space for Continuum Robots

Guoqing Zhang and Long Wang

Abstract—In continuum robotics, real-time robust shape estimation is crucial for planning and control tasks that involve physical manipulation in complex environments. In this paper, we present a novel stochastic observer-based shape estimation framework designed specifically for continuum robots. The shape state space is uniquely represented by the modal coefficients of a polynomial, enabled by leveraging polynomial curvature kinematics to describe the curvature distribution along the arclength. Our framework processes noisy measurements from limited discrete position, orientation, or pose sensors to estimate the shape state robustly. We derive a novel noise-weighted observability matrix, providing a detailed assessment of observability variations under diverse sensor configurations. To overcome the limitations of a single model, our observer employs the Interacting Multiple Model (IMM) method, coupled with Extended Kalman Filters (EKFs), to mix polynomial curvature models of different orders. The IMM approach, rooted in Markov processes, effectively manages multiple model scenarios by dynamically adapting to different polynomial orders based on real-time model probabilities. This adaptability is key to ensuring robust shape estimation of the robot’s behaviors under various conditions. Our comprehensive analysis, supported by both simulation studies and experimental validations, confirms the robustness and accuracy of our proposed methods.

Index Terms—Shape estimation, Continuum robots, Extended Kalman filter, Interacting multiple model, polynomial curvature kinematics, Observability analysis

I. INTRODUCTION

Inspired by biological features such as an elephant’s trunk or an octopus’s tentacles, continuum robots are an unconventional class of robots that have inherent large degrees of flexibility, underactuation, and compliance. Such “soft” features allow them to have safe physical interactions with the environments [1]. With recent advances in instrument miniaturization, continuum robot designs have been widely used in many minimally invasive surgery applications [2], [3], and their advantages are further leveraged for safe manipulation and access to deep anatomy.

Robustly ascertaining the shape of continuum robots is critical for effective motion planning and control. This task typically involves a comprehensive shape estimation framework integrating sensing techniques, representation methods, and estimation approaches.

G. Zhang and L. Wang are with the Department of Mechanical Engineering, Stevens Institute of Technology, New Jersey, NJ, 07030, USA, e-mail: lwang4@stevens.edu

This work was supported in part by USDA-NIFA Grant No. 2021-67022-35977 and by Stevens Institute of Technology internal grants.

A. Sensing Technique

Shape sensing is pivotal in this context by supplying the observational data critical for robust shape estimation. A diverse array of sensing techniques is deployed to acquire the shape information. External sensing involves equipping robots with sensors such as Electromagnetic (EM) sensors [4–9], vision-based systems [7], [10], [11], or Inertial measurement units (IMUs) [12], [13] to obtain pose information externally. Alternatively, intrinsic sensing leverages internal sensors to enhance joint-level information, utilizing encoders or passive cable displacement measurements [14]. Given their infinite degrees of freedom (DoF), the challenge with continuum robots lies in capturing comprehensive pose information along their entire length with a finite number of sensors. While technologies like Fiber Bragg Grating (FBG) sensors [9], [15–19] and vision-based systems can map out the full robot shape, constraints such as budget and the specific requirements of the application often preclude their ubiquitous use.

B. Representations in Modeling

Different shape representation methods yield various formulations of the backbone curvature, which directly impact continuum robots’ computed position and orientation. Representation methods can be categorized as distributed and lumped parameterizations for the backbone curvature [20], [21].

Distributed parameterization methods represent the backbone curvature as a continuous function of the arc length, characterized by an infinite number of parameters. These methods assume that the curvature distribution is variable along the length of the robot. A classic example is the Cosserat rod model, which employs distributed parameter modeling to account for the underlying mechanics by solving for positional, force, and moment boundary conditions [22–26].

Lumped parameterization uses a finite set of parameters to describe the backbone shape of continuum robots geometrically. This approach primarily includes three methods: the Pseudo-Rigid-Body Model (PRBM), the constant curvature (CC) assumption, and the modal approach [20]. PRBM approximates the central backbone shape of continuum robots as a series of rigid links connected by torsion springs [27–30]. The constant curvature (CC) model assumes that each segment of the continuum robot follows a constant curvature, typically represented as a circular arc, with a single curvature parameter defining the shape. Due to its simplification and computation efficiency, it is deployed quickly for ideal situations such

as uniform mass/material distribution, frictionless transmission, and free from external loading. As a widely adopted kinematics-based approach, The CC model is extensively used in applications ranging from surgical procedures [31–34] and field operations [35] to underwater exploration [36] and aerial maneuvers [37]. In contrast, the modal approach [38] represents backbone curvature as a linear combination of modal shape functions (e.g., monomials [39], Euler curves [40], Chebyshev polynomials [14], and polynomial curvature kinematics [12], [41]). A modal approach offers the advantage of capturing complex, continuous deformations with a relatively small number of parameters, making it computationally efficient while still maintaining high accuracy in shape representation.

C. Estimation Approach

Various sensing techniques and representation methods drive multiple estimation approaches tailored to the specific scenario. In static configurations, where the continuum robot remains stationary and its state does not change over time, researchers often employ curve fitting or optimization methods based on modal approaches [4], [14], [15], [40], and the Pseudo Rigid Body Model (PRBM) [10]. Considering model uncertainty and measurement noise, Lilge et al. [6] and Ferguson et al. [42] implemented Gaussian Process Regression for static shape estimation under arclength domain using the Cosserat rod model.

Dynamic configurations involve continuous state updates as the continuum robot moves and its state changes over time. In such scenarios, stochastic observer-based estimation methods, particularly filtering approaches, are preferred for their ability to optimize state estimation by balancing the influences of process and measurement models, where noise from both sources significantly impacts accuracy and robustness. Although the Extended Kalman Filter (EKF) is commonly employed in dynamic shape estimation, it predominantly relies on constant curvature (CC) or piecewise constant curvature (PCC) models [8], [11], [13]. These models generally focus on estimating the tip pose or bending angles, with less attention to the entire curvature distribution along the structure. Despite this, more advanced techniques like the Unscented Kalman Filter and Dual Particle Filter have been successfully applied to enhance the CC/PCC models, offering a broader dynamic shape estimation capability [7], [43].

D. Key Gaps in Shape Estimation Methods

Despite significant advancements in shape estimation for continuum robots, several critical challenges remain.

Gap 1: Traditional estimation methods, particularly those based on simpler models like constant curvature (CC) or piecewise constant curvature (PCC), typically focus on estimating the pose in task space and/or the state in joint space. However, there is a significant gap in these approaches as they do not capture the shape state in curvature space, which is more closely aligned with the robot’s natural mechanics and physical properties. This gap limits the accuracy and relevance of the

estimations, especially in applications that require a deeper understanding of the robot’s internal dynamics and external interactions.

Gap 2: Representing the state in curvature space, particularly with polynomial curvature models, introduces challenges due to the nonlinear dynamics and the risk of overfitting or underfitting across different model orders. These complexities complicate the direct adoption of conventional stochastic observer methods, such as EKF and UKF, which typically rely on a single model for state estimation.

Gap 3: Current approaches also inadequately optimize sensor configurations using conventional observability analysis, often overlooking sensor noise characteristics, which leads to suboptimal sensor placement.

E. Contributions of This Work

To address the challenges in dynamic shape estimation across various types of continuum robots, we propose a pioneering stochastic observer-based framework that utilizes general pose, position, and orientation sensing techniques combined with polynomial curvature kinematics, with a particular focus on cable-driven continuum robots (illustrated in Fig. 1). The principal contributions of our research include:

- To the best of our knowledge, we are the first to introduce a stochastic observer in polynomial curvature shape state space: This novel approach significantly enhances real-time estimation accuracy and robustness by utilizing the modal coefficients space as the shape state space.
- Introduction of Adaptive Estimation Approaches: We are the first to implement adaptive IMM-EKF methods in the field of shape estimation. These methods enhance the adaptability and robustness of our models within dynamic environments.
- Innovative Noise-Weighted Observability Matrix: Our framework introduces this critical tool for the first time, assessing observability under various sensor configurations. By incorporating sensor noise characteristics, it strategically optimizes sensor placement for maximum observability, thus enhancing the reliability and effectiveness of estimations.
- Comprehensive Simulations and Experimental Validations: These substantiate the effectiveness of our innovative approaches. Results confirm our methods’ practical utility and performance enhancement over existing methods.

II. PROBLEM FORMULATION

To develop a robust stochastic observer-based shape estimation framework for continuum robots, enhancing their functionality in dynamic and unpredictable environments, four specific problems need to be addressed, which are framed around the following foundational equations:

$$\dot{\mathbf{m}}(t) = \mathbf{f}(\mathbf{m}(t), \mathbf{u}(t)) \quad (1)$$

$$\mathbf{y}(t) = \mathbf{h}(\mathbf{m}(t)) \quad (2)$$

$$\hat{\mathbf{m}}(t) = \text{Observer_Method}(\cdot) \quad (3)$$

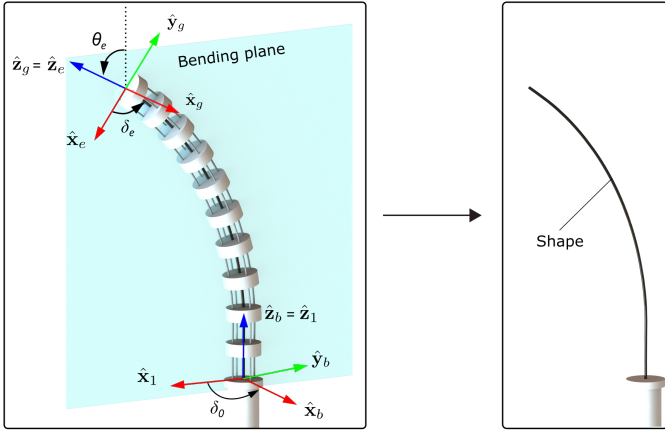


Fig. 1: The illustration of a cable-driven continuum robot and the shape of its central backbone.

where

- t represents time,
- $\mathbf{m}(t)$ is the robot's shape state vector, containing variables that describe the shape of the robot,
- $\mathbf{u}(t)$ denotes the system input,
- $\mathbf{y}(t)$ is the output vector, which can be directly measured from the system,
- $\dot{\mathbf{m}}(t)$ denotes the derivative of $\mathbf{m}(t)$ with respect to time, describing the system's dynamics,
- \mathbf{f} is a vector function defining the state dynamics, depending on the current state and input,
- \mathbf{h} is a measurement function mapping the state space to the measurement space,
- $\hat{\mathbf{m}}(t)$ is the estimate of the shape state,
- `Observer_Method(.)` denotes the observer algorithm employed to estimate the state vector from the measurements and the process model.

These problems include:

- 1) *Shape state representation*: Defining a compact and computationally efficient shape state vector $\mathbf{m}(t)$ that can accurately capture the dynamic properties of the continuum robot. Polynomial curvature kinematics is utilized to address this problem(details are provided in Section III-A).
- 2) *Process model development*: Constructing a process model that accurately describes the dynamics of the robot's shape changes over time, influenced by control inputs $\mathbf{u}(t)$ and inherent system noise. This model builds upon the state transition equation (1)(the detailed derivation is available in Section III-C) with process noises.
- 3) *Measurement model construction*: Creating a measurement model that maps the shape state to observable outputs, ensuring that this model accounts for potential measurement noise. This model is constructed based on the output equation (2)(the detailed derivation is presented in Section III-D) with sensor noises.
- 4) *stochastic observer design*: architecting an adaptive recursive estimation approach (equation 3) to accurately esti-

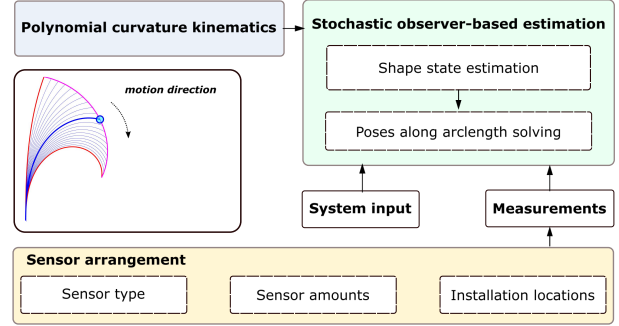


Fig. 2: Diagram of proposed shape estimation method

mate the shape state based on the process and measurement models. Interacting multiple models (IMM) coupled with Extended Kalman filters (EKFs) are employed to address this challenge (detailed discussions are illustrated in Section IV).

The detailed workflow of the proposed shape estimation methodology is depicted in Fig. 2. This workflow specifically focuses on the in-plane bending motion of a single continuum segment and utilizes limited position and/or orientation measurements from sensors located at strategic points. These sensors include off-the-shelf devices such as Electro-Magnetic (EM) sensors, Inertia Measurement Units (IMU), and cameras, etc., making our approach widely accessible for researchers. The integration of previous shape states and a process model, based on polynomial curvature kinematics, with measurements from these sensors, feeds into a real-time recursive shape estimation method. This method provides the optimal estimate of the shape state and all corresponding poses along the arc length. Additionally, a comprehensive observability analysis for different sensor configurations is conducted using the proposed noise-weighted observability matrix (detailed in section V). An extensive simulation study and experimental validations are discussed in section VI and section VII, respectively.

III. MODEL FORMULATION FOR OBSERVER DESIGN

This section delineates the development of the shape state, state transition model, and measurement model, all of which are based on polynomial curvature kinematics. The nomenclature used in these kinematic models is summarized in Table I.

A. Polynomial Curvature Kinematics

Before we delve into the kinematics model, it's crucial to establish some assumptions to contextualize this problem. The following assumptions are posited:

- (1) *Planar Bending Assumption*: The robot's bending motion is strictly planar, negating any out-of-plane deformations.
- (2) *Inextensibility of Backbone*: The robot's backbone length remains invariant regardless of its bending configuration.

A precise representation and model of the shape for continuum robots([41], [12]) is rooted in polynomial curvature kinematics. Leveraging this model, all the poses spanning

the arclength can be ascertained by integrating a curvature function. The general curvature function is described as an infinite expansion of monomials:

$$\kappa(s, t) = \sum_{i=0}^{\infty} m_i(t) s^i, \quad s \triangleq \frac{l}{L}, \quad s \in [0, 1] \quad (4)$$

where s is a normalized arclength coordinate, t is the time, m_i represents the modal coefficient of i^{th} -order, l denotes the arclength, and L is the constant central-backbone length.

1) *Finite Dimension Approximation*: A finite-dimensional approximation of equation 4 with highest order j can be expressed as:

$$\kappa(s, t) \simeq \sum_{i=0}^j m_i(t) s^i \quad (5)$$

The accuracy of representing a continuum robot's shape is closely related to the order of the curvature function employed. A higher-order curvature function can capture the robot's shape with greater precision. However, this comes at the cost of increased complexity due to the inclusion of additional high-order terms.

2) *Forward kinematics of configuration-to-task space*: The bending angle $\theta(s, t)$ at the normalized arclength s can be obtained by integrating the above curvature equation.

$$\theta(s, t) = \int_0^s \kappa(\tau, t) d\tau = \sum_{i=0}^j m_i(t) \frac{s^{i+1}}{i+1} \quad (6)$$

In this paper, we assume no torsional twist happened along the backbone length. Therefore, the robot shape can be fully observed in Frame {1}. If there is no specific instruction, all vectors are described in Frame {1}. Figure 3 shows the derivation of the in-plane bending kinematics. Let $\mathbf{p}(s)$ be the position at normalized arclength s in task space. The tangent unit vector is derived as:

$$\mathbf{e}_t \triangleq \frac{d\mathbf{p}}{dl} = \frac{d\mathbf{p}}{d(sL)} = [\sin(\theta(s, t)), 0, \cos(\theta(s, t))]^T \quad (7)$$

Then, the position vector $\mathbf{p}(s)$ is expressed by the integral of $\frac{d\mathbf{p}}{ds}$ along the normalized arclength s :

$$\begin{aligned} \mathbf{p}(s) &\triangleq [p_x(s), p_y(s), p_z(s)]^T \\ &= \int_0^s L [\sin(\theta(\tau, t)), 0, \cos(\theta(\tau, t))]^T d\tau \end{aligned} \quad (8)$$

Combining with the bending angle $\theta(s, t)$, the bending direction angle $\delta(t)$ and the position vector $\mathbf{p}(s)$, the homogeneous transformation at location s can be obtained:

$${}^b\mathbf{T}_{g_s}(s, t) = {}^b\mathbf{T}_1 {}^1\mathbf{T}_{e_s} {}^{e_s}\mathbf{T}_{g_s} \quad (9)$$

where

$${}^b\mathbf{T}_1 = \begin{bmatrix} \text{RotZ}(-\delta(t)) & \mathbf{0} \\ \mathbf{0} & 1 \end{bmatrix} \quad (10)$$

$${}^1\mathbf{T}_{e_s} = \begin{bmatrix} \text{RotY}(\theta(s, t)) & \mathbf{p}(s) \\ \mathbf{0} & 1 \end{bmatrix} \quad (11)$$

$${}^{e_s}\mathbf{T}_{g_s} = \begin{bmatrix} \text{RotZ}(\delta(t)) & \mathbf{0} \\ \mathbf{0} & 1 \end{bmatrix} \quad (12)$$

B. Shape State Representation

In conventional continuum robot modeling, the state is typically represented by configuration space variables such as the tip bending angle θ_e and the bending plane angle δ , based on a constant curvature model:

$$\boldsymbol{\psi} \triangleq [\theta_e, \delta]^T \quad (13)$$

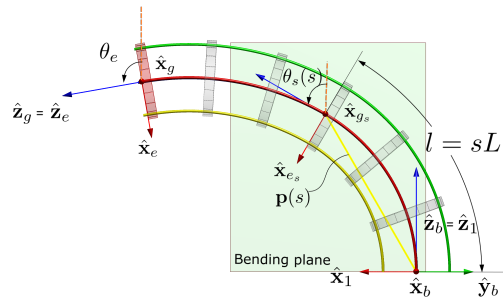


Fig. 3: Schematic of in-plane bending kinematics

TABLE I: Kinematics Nomenclature

| Symbol | Description |
|-------------------------------------|--|
| $s \in [0, 1]$ | Normalized arclength coordinate of one continuum segment |
| L | Central backbone length of continuum segment |
| l | Arclength coordinate at location s |
| $\kappa(s, t)$ | Curvature at location s and time t |
| $m_i(t)$ | Modal coefficient of order i at time t |
| $\theta(s, t)$ | Bending angle at location s and time t |
| θ_e | Bending angle at tip, $\theta_e = \theta(1, t)$ |
| $\delta(t)$ | Bending plane angle at time t |
| $\boldsymbol{\psi}$ | Robot state defined by configuration space variables |
| \mathbf{m} | Shape state defined by the modal coefficients vector |
| $\mathbf{J}_{\psi\mathbf{m}}$ | <i>configuration-to-shape</i> space Jacobian |
| $\mathbf{J}_{\mathbf{h}\mathbf{m}}$ | <i>task-to-shape</i> space Jacobian |
| Frame {F} | designates a right-handed frame with unit vectors $\hat{\mathbf{x}}_f, \hat{\mathbf{y}}_f, \hat{\mathbf{z}}_f$ and point \mathbf{f} as its origin. |
| Frame {B} | defines the base frame with \mathbf{b} located at the center of the base disk, $\hat{\mathbf{x}}_b$ passing through the first secondary backbone and $\hat{\mathbf{z}}_b$ perpendicular to the base disk. |
| Frame {1} | characterizes the bending plane and is obtained by a rotation of $(-\delta_0)$ about $\hat{\mathbf{z}}_b$ from Frame {B} |
| Frames {Es} & {Gs} | Frame {Gs} and Frame {Es} are attached to the axial center of the central backbone at length s . The x-axis of {Es} is the intersection of the bending plane and the orthogonal plane of the central backbone. Frame {Gs} is obtained by a rotation $\delta(s, t)$ about $\hat{\mathbf{z}}_{e_s}$ from {Es}. |
| Frames {E} & {G} | Frame {G} and Frame {E} are attached to the top surface of end disk. These frames are Frame {Gs} and Frame {Es} when $s = 1$. |

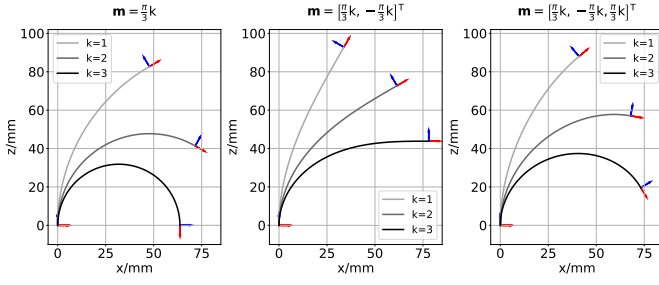


Fig. 4: Bending shapes generated on a central backbone with $L = 100\text{mm}$ by using different order curvature polynomials.

However, this model assumes uniform curvature along the robot's length and simplifies the representation, which often does not accurately reflect the complex shape dynamics in environments with disturbances. Additionally, since this work focuses exclusively on in-plane bending motions, we omit the bending plane angle δ from our analysis, further simplifying the model to better suit our specific research needs.

To enhance accuracy and adaptability in representing the robot's shape, we adopt a modal coefficients representation. By defining the shape state vector \mathbf{m} as:

$$\mathbf{m} \triangleq [m_0, \dots, m_j]^\top, \mathbf{m} \in \mathbb{R}^{(j+1) \times 1} \quad (14)$$

We introduce a scalable method where increasing the order j of modal coefficients allows for a more precise depiction of the robot's in-plane shape. This approach enhances the fidelity of the shape representation and provides comprehensive shape information, thereby surpassing the accuracy achievable with just the tip bending angle. Some sample shapes represented by 0^{th} , 1^{st} and 2^{nd} polynomials are demonstrated in Fig. 4.

C. State Transition Model

The scope of our work is confined to evaluating the proposed observer-based shape estimation framework. Consequently, we do not incorporate advanced control strategies but instead opt for a straightforward open-loop control. The control input \mathbf{u} is designated as the change in the bending angle at the tip, denoted by $\delta\theta_e$.

To establish the state transition model, it is essential to delineate the relationship between the change in shape state and the bending angle. By setting $s = 1$, the relationship is expressed through the following mapping derived from equation (6):

$$\delta\theta_e = \mathbf{J}_{\psi\mathbf{m}} \delta\mathbf{m} \quad (15)$$

$$\mathbf{J}_{\psi\mathbf{m}} = \frac{\partial\theta(1, t)}{\partial\mathbf{m}} = \left[1, \frac{1}{2}, \dots, \frac{1}{j+1} \right] \quad (16)$$

where $\mathbf{J}_{\psi\mathbf{m}}$ is *configuration-to-shape* space Jacobian, facilitating the mapping from modal coefficients to bending angle changes.

Subsequently, the infinitesimal change in the shape state is given by:

$$\delta\mathbf{m} = \mathbf{J}_{\psi\mathbf{m}}^\dagger \delta\theta_e \quad (17)$$

Here, $\mathbf{J}_{\psi\mathbf{m}}^\dagger$ represents the Moore-Penrose pseudoinverse of $\mathbf{J}_{\psi\mathbf{m}}$, computed as: $\mathbf{J}_{\psi\mathbf{m}}^\dagger = \mathbf{J}_{\psi\mathbf{m}}^\top (\mathbf{J}_{\psi\mathbf{m}} \mathbf{J}_{\psi\mathbf{m}}^\top)^{-1}$.

The discrete-time model for the state transition, used at time step k , is thus formulated as:

$$\begin{aligned} \mathbf{m}_k &= \mathbf{f}(\mathbf{m}_{k-1}, \mathbf{u}_k) = \mathbf{m}_{k-1} + \delta\mathbf{m}_k \\ \delta\mathbf{m}_k &= \mathbf{J}_{\psi\mathbf{m}}^\dagger \delta\theta_{ek} = \mathbf{J}_{\psi\mathbf{m}}^\dagger \mathbf{u}_k \end{aligned} \quad (18)$$

This equation represents the discrete-time format of the state transition model, as stipulated in equation (1).

D. Measurement Model

This section outlines the measurement model that integrates the in-plane position and bending angle for a pose sensor located at location s and time t . The model is formulated as:

$$\begin{aligned} \mathbf{y}_p(s, t) &= [p_x(s, t), p_z(s, t), \theta(s, t)]^\top \\ &= \left[L \int_0^s \sin(\theta(\tau, t)) d\tau, L \int_0^s \cos(\theta(\tau, t)) d\tau, \theta(s, t) \right]^\top \end{aligned} \quad (19)$$

where (p_x, p_z) denotes the \mathbf{x} and \mathbf{z} coordinates of the sensor in Frame $\{1\}$.

Considering the variability in the number and location of sensors, the measurement model is extended to accommodate the entire array of sensors, thus being represented as a function of the shape state \mathbf{m} :

$$\mathbf{h}_p(\mathbf{m}) \triangleq [\mathbf{y}_p(s_0, t)^\top, \dots, \mathbf{y}_p(s_n, t)^\top]^\top, \mathbf{h}_p \in \mathbb{R}^{3(n+1) \times 1} \quad (20)$$

where $n+1$ represents the number of sensors.

To support the shape estimation framework and given that the measurements are in *task* space, we derive the *task-to-shape* space Jacobian, denoted as $\mathbf{J}_{\mathbf{h}\mathbf{m}}$. To simplify its final expression, we introduce a function $\mathbf{G}(s, t)$ as:

$$\begin{aligned} \mathbf{G}(s, t) &\triangleq \frac{\partial\mathbf{y}_p(s, t)}{\partial\mathbf{m}}, \mathbf{G}(s, t) \in \mathbb{R}^{3 \times (j+1)} \\ &= \begin{bmatrix} \frac{\partial p_x(s, t)}{\partial m_0} & \dots & \frac{\partial p_x(s, t)}{\partial m_i} & \dots & \frac{\partial p_x(s, t)}{\partial m_j} \\ \frac{\partial p_z(s, t)}{\partial m_0} & \dots & \frac{\partial p_z(s, t)}{\partial m_i} & \dots & \frac{\partial p_z(s, t)}{\partial m_j} \\ \frac{\partial\theta(s, t)}{\partial m_0} & \dots & \frac{\partial\theta(s, t)}{\partial m_i} & \dots & \frac{\partial\theta(s, t)}{\partial m_j} \end{bmatrix} \end{aligned} \quad (21)$$

where

$$\frac{\partial p_x(s, t)}{\partial m_i} = L \int_0^s \cos(\theta(\tau, t)) \frac{\tau^{i+1}}{i+1} d\tau \quad (22)$$

$$\frac{\partial p_z(s, t)}{\partial m_i} = L \int_0^s -\sin(\theta(\tau, t)) \frac{\tau^{i+1}}{i+1} d\tau \quad (23)$$

$$\frac{\partial\theta(s, t)}{\partial m_i} = \frac{s^{i+1}}{i+1} \quad (24)$$

Finally, $\mathbf{J}_{\mathbf{h}\mathbf{m}}$ is defined as:

$$\begin{aligned} \mathbf{J}_{\mathbf{h}\mathbf{m}} &\triangleq \frac{\partial\mathbf{h}_p(\mathbf{m})}{\partial\mathbf{m}}, \mathbf{J}_{\mathbf{h}\mathbf{m}} \in \mathbb{R}^{3(n+1) \times (j+1)} \\ &= [\mathbf{G}(s_0, t)^\top, \dots, \mathbf{G}(s_n, t)^\top]^\top \end{aligned} \quad (25)$$

Adjustments to the measurement model may be necessary depending on the specific sensor types used (position or

orientation sensors) and their configurations. Variations in sensor arrangement necessitate corresponding modifications in the measurement model and its Jacobian matrix.

IV. IMM-EKF DESIGN

The Extended Kalman Filter (EKF) is a robust, real-time state estimation technique for nonlinear systems, widely acclaimed for its effectiveness. However, the complex dynamic behaviors of continuum robots often render single-model approaches inadequate. The Interacting Multiple Model (IMM) method addresses this limitation by enabling seamless transitions between multiple models, thereby capturing the evolving shape of continuum robots in various situations.

In this study, we utilize three polynomial curvature models of different orders: 0th order, 1st order, and 2nd order, positing that the 2nd order polynomial provides the highest fidelity. Although the 2nd order polynomial offers greater precision, it may overfit and exhibit increased sensitivity to noise in simpler environments where a lower-order model could prove more robust.

To circumvent issues of overfitting while ensuring flexibility and precision, we integrate the IMM with the EKF, creating an optimal fusion of polynomial curvature models. This approach enhances robust shape estimation across diverse operational conditions. Our proposed IMM-EKF methodology introduces a novel strategy for shape estimation in continuum robots, significantly improving accuracy and adaptability.

In the subsequent sections, we revisit the standard IMM method and introduce our refined approach. We address two key challenges in the model interaction stage to enhance overall performance. The main nomenclature for the observer design is illustrated in Table II.

A. IMM Formulation

The schematic of the IMM-EKF algorithm is depicted in Fig. 5. The IMM algorithm progresses through three distinct stages in each cycle: interaction, filtering, and combination. The interaction stage sets the initial conditions for each model's filter by merging the state estimates from the previous time step. This is followed by the filtering stage, where prediction and update operations are carried out simultaneously across all models. The cycle concludes with the combination stage, where the updated state estimates from all filters are integrated into a unified state estimate through a weighted sum, using the updated model probabilities. Detailed mathematical formulations for each stage are provided in the subsequent sections.

1) *Multiple Model Set*: We denote a system model using i^{th} order of polynomial curvature function as $M^{(i)} \in \mathbb{M} = \{M^{(0)}, M^{(1)}, \dots, M^{(r)}\}$. The discrete-time process and measurement models for $M^{(i)}$ are defined as:

$$\begin{aligned} \mathbf{m}_k^{(i)} &= \mathbf{f}(\mathbf{m}_{k-1}^{(i)}, \mathbf{u}_{k-1}) + \mathbf{v}_{k-1}^{(i)} \\ \mathbf{y}_k &= \mathbf{h}_p(\mathbf{m}_k^{(i)}) + \mathbf{n}_k^{(i)} \end{aligned} \quad (26)$$

where \mathbf{f} denotes the state transition model detailed in III-C, \mathbf{h}_p represents the measurement model function derived in III-D;

TABLE II: IMM-EKF Nomenclature

| Symbol | Description |
|---------------------------------|--|
| $M^{(i)}$ | System model using i^{th} order of polynomial curvature function |
| \tilde{V}_k | Predicted value of variable V at time k given the measurements up to time $k-1$ |
| \hat{V} | Estimated value of variable V after correction stage of filtering |
| \mathbf{P} | Markov probability transition matrix |
| p_{ij} | Probability of transitioning from $M^{(i)}$ at time $k-1$ to $M^{(j)}$ at time k |
| $P(A B)$ | Probability of event A, given event B |
| $\mu_{k-1}^{(j) (i)}$ | The mixing probability at time $k-1$ for $M^{(j)}$ given that $M^{(i)}$ is assumed to be the correct model at time k . This mixing probability is used to incorporate information from different models. |
| $\mu_k^{(i)}$ | The probability of $M^{(i)}$ at time k given all observations up to time k |
| $\tilde{\mu}_k^{(i)}$ | The priori (predicted) model probability at time k for $M^{(i)}$, given all observations up to time $k-1$ |
| $\hat{\mathbf{m}}_{k-1}^{(0i)}$ | Mixed initial state vector of $M^{(i)}$ |
| $\hat{\mathbf{C}}_{k-1}^{(0i)}$ | Mixed initial covariance matrix of $M^{(i)}$ |
| $\Lambda_k^{(i)}$ | The probability of observing \mathbf{y}_k , given all previous observations and assuming $M^{(i)}$ is the correct model. |
| $\mathcal{N}(x; \mu, \Sigma)$ | The Gaussian probability density function with mean μ and covariance Σ |
| ν_r | simulated position noise |
| ν_ψ | simulated bending angle noise |
| $\hat{\mathbf{m}}_0^j$ | initial estimated state of $M^{(j)}$ |
| $\hat{\mathbf{C}}_0^j$ | initial state covariance of $M^{(j)}$ |
| \mathbf{Q} | state process covariance |
| \mathbf{R} | state measurement covariance |
| $\mathbf{F}_k^{(i)}$ | State transition matrix of i^{th} EKF at time step k |
| $\mathbf{H}_k^{(i)}$ | Observation matrix of i^{th} EKF at time step k |
| $\mathbf{S}_k^{(i)}$ | innovation (or residual) covariance of i^{th} EKF at time step k |
| $\mathbf{K}_k^{(i)}$ | near-optimal Kalman gain of i^{th} EKF at time step k |

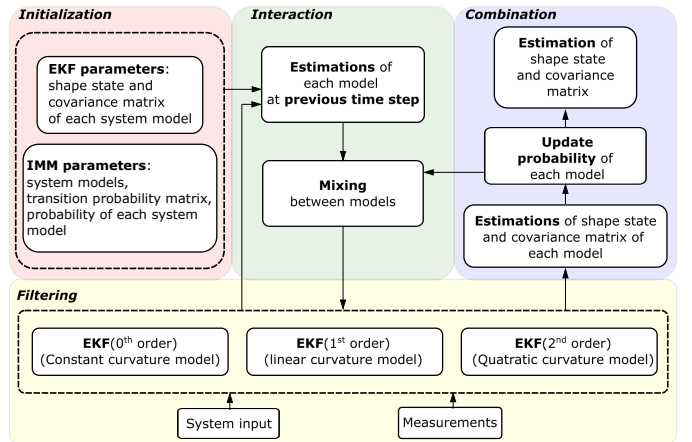


Fig. 5: Schematic of IMM-EKF algorithm

\mathbf{y}_k is the measurement at time step k ; \mathbf{v}_{k-1} and \mathbf{n}_k are independent Gaussian noise processes with means $\bar{\mathbf{v}}$ and $\bar{\mathbf{n}}$, and covariance matrices \mathbf{Q} and \mathbf{R} , respectively.

Note that the set \mathbb{M} is time-invariant, and for this study, we employ three models, hence $r = 2$.

2) *Probability transition matrix*: The Markov transition probability matrix (TPM), denoted as \mathbf{P} , encapsulates the probabilities of transitioning from one model to another between consecutive time steps. Each element p_{ij} within \mathbf{P} specifies the *priori* probability of transitioning from model i at time $k-1$ to model j at time k . The matrix is formulated as follows:

$$\mathbf{P} = \begin{bmatrix} p_{00} & \cdots & p_{0r} \\ \cdots & p_{ij} & \cdots \\ p_{r0} & \cdots & p_{rr} \end{bmatrix} \quad (27)$$

$$\sum_{j=0}^r p_{ij} = 1, 0 \leq p_{ij} \leq 1 \quad (28)$$

3) *State Interaction / Mixing*: To set up the inputs for the filtering process of each model at a new time step, the algorithm calculates mixing probabilities. These probabilities are used to establish the initial state and covariance estimates for each model, factoring in the probability of transitions from all other models in the previous time step.

The mixing probability of transitioning from model j to i is calculated by:

$$\mu_{k-1}^{(j)|(i)} = \frac{p_{ji}\mu_{k-1}^{(j)}}{\check{\mu}_k^{(i)}}, \quad \check{\mu}_k^{(i)} = \sum_{j=0}^r p_{ji}\mu_{k-1}^{(j)} \quad (29)$$

The mathematic derivation is detailed in Appendix B.

For each model i , the mixed initial state estimate and the mixed initial error covariance are computed by aggregating all state estimates and covariance matrices from the previous time step, weighted by the mixing probabilities. These calculations also include terms that account for the differences between each model's estimate and the mixed estimate, reflecting the uncertainty in the state estimate due to potential model switching. The formulas are as follows:

$$\hat{\mathbf{m}}_{k-1}^{(0i)} = \sum_{j=0}^r \mu_{k-1}^{(j)|(i)} \hat{\mathbf{m}}_{k-1}^{(j)} \quad (30)$$

$$\hat{\mathbf{C}}_{k-1}^{(0i)} = \sum_{j=0}^r \mu_{k-1}^{(j)|(i)} \left(\hat{\mathbf{C}}_{k-1}^{(j)} + \left(\hat{\mathbf{m}}_{k-1}^{(j)} - \hat{\mathbf{m}}_{k-1}^{(0i)} \right) \left(\hat{\mathbf{m}}_{k-1}^{(j)} - \hat{\mathbf{m}}_{k-1}^{(0i)} \right)^\top \right) \quad (31)$$

4) *Mode-Matched Filtering*: In the IMM approach, mode-matched filtering is a pivotal step where each candidate model's filter operates independently but in parallel. This stage begins by initializing each filter with the mixed initial conditions derived from the interaction stage. This parallel operation allows the IMM to maintain a robust set of hypotheses about the system's state, ready to adjust based on incoming measurements.

The prediction for each model i is calculated as follows:

$$\check{\mathbf{m}}_k^{(i)} = \mathbf{f} \left(\hat{\mathbf{m}}_{k-1}^{(0i)}, \mathbf{u}_k \right) \quad (32)$$

$$\check{\mathbf{C}}_k^{(i)} = \mathbf{F}_k^{(i)} \hat{\mathbf{C}}_{k-1}^{(0i)} \left(\mathbf{F}_k^{(i)} \right)^\top + \mathbf{Q}^{(i)} \quad (33)$$

The correction step refines the state and covariance estimates based on the latest measurements:

$$\mathbf{S}_k^{(i)} = \mathbf{H}_k^{(i)} \check{\mathbf{C}}_k^{(i)} \left(\mathbf{H}_k^{(i)} \right)^\top + \mathbf{R}^{(i)} \quad (34)$$

$$\mathbf{K}_k^{(i)} = \check{\mathbf{C}}_k^{(i)} \left(\mathbf{H}_k^{(i)} \right)^\top \left(\mathbf{S}_k^{(i)} \right)^{-1} \quad (35)$$

$$\hat{\mathbf{m}}_k^{(i)} = \check{\mathbf{m}}_k^{(i)} + \mathbf{K}_k^{(i)} \left(\mathbf{y}_k - \mathbf{h}_p \left(\check{\mathbf{m}}_k^{(i)} \right) \right) \quad (36)$$

$$\hat{\mathbf{C}}_k^{(i)} = \left(\mathbf{I} - \mathbf{K}_k^{(i)} \mathbf{H}_k^{(i)} \right) \check{\mathbf{C}}_k^{(i)} \quad (37)$$

5) *Model Likelihood/probability Update*: After the filtering stage, it is crucial to update the likelihood of model i as well as its model probability based on the new measurement at time k . The likelihood of model i is computed using the multivariate Gaussian distribution:

$$\Lambda_k^{(i)} = \mathcal{N} \left(\mathbf{y}_k - \mathbf{h}_p \left(\check{\mathbf{m}}_k^{(i)} \right); \mathbf{0}, \mathbf{S}_k^{(i)} \right) \quad (38)$$

The model probability of model i at time k given all the measurements up to time k can be calculated based on Bayes' theorem:

$$\mu_k^{(i)} = \frac{\check{\mu}_k^{(i)} \Lambda_k^{(i)}}{\sum_{j=0}^r \check{\mu}_k^{(j)} \Lambda_k^{(j)}} \quad (39)$$

Detailed mathematical derivations of these formulas are provided in Appendix C.

6) *Model Combinations*: In the final step of the IMM algorithm, we aggregate the estimates from all models to derive the optimal overall estimate of the system state at time k :

$$\hat{\mathbf{m}}_k = \sum_{i=0}^r \mu_k^{(i)} \hat{\mathbf{m}}_k^{(i)} \quad (40)$$

The combined covariance of the estimate, which quantifies the estimated accuracy and uncertainty of the state estimate, is computed as follows:

$$\hat{\mathbf{C}}_k = \sum_{i=0}^r \mu_k^{(i)} \left(\hat{\mathbf{C}}_k^{(i)} + \left(\hat{\mathbf{m}}_k - \hat{\mathbf{m}}_k^{(i)} \right) \left(\hat{\mathbf{m}}_k - \hat{\mathbf{m}}_k^{(i)} \right)^\top \right) \quad (41)$$

B. Refining IMM

However, the standard IMM framework exhibits two primary limitations. First, it struggles with the mixing of state vectors with unequal dimensions. In such cases, the mixing stage may introduce biases when smaller-dimensional state vectors are combined with larger ones, potentially leading to inaccuracies in state estimation and model predictions. Second, the conventional IMM uses a fixed Transition Probability Matrix (TPM) predefined based on prior assumptions about system dynamics. This static approach fails to accommodate environmental or internal disturbances that could dynamically

alter system behavior, thus limiting IMM's effectiveness in unpredictable scenarios.

To overcome these issues, we propose a refined technique for managing state vectors of different dimensions and incorporates an adaptive mechanism for adjusting the TPM, making it more responsive to changes in the system's conditions.

1) *Mitigating Bias in State Dimensionality*: In the mixing stage of the IMM, the mixed initial state for each model is derived based on Equation (31), which requires uniform dimensionality across all state vectors and their corresponding covariance matrices. The conventional IMM approach often addresses dimensional discrepancies by setting augmented components in state vectors with smaller dimensions to zero. This leads to potential biases in the mixed initial states of models with larger dimensions. Inspired by [44], which provides an unbiased mixing solution for two models, we propose an unbiased mixing strategy tailored for multiple models with varying dimensions, illustrated using the case of $\mathbb{M} = \{M^{(0)}, M^{(1)}, M^{(2)}\}$.

Consider the state vector and covariance matrix of $M^{(2)}$ as follows:

$$\hat{\mathbf{m}}^{(2)} = \begin{bmatrix} \hat{m}_0^{(2)} \\ \hat{m}_1^{(2)} \\ \hat{m}_2^{(2)} \end{bmatrix}, \hat{\mathbf{C}}^{(2)} = \begin{bmatrix} C_0^{(2)} & C_{01}^{(2)} & C_{02}^{(2)} \\ C_{10}^{(2)} & C_1^{(2)} & C_{12}^{(2)} \\ C_{20}^{(2)} & C_{21}^{(2)} & C_2^{(2)} \end{bmatrix} \quad (42)$$

The corresponding state vectors and covariance matrices for $M^{(1)}$ and $M^{(0)}$ are defined similarly but with reduced dimensions.

To ensure dimensional consistency and unbiased mixing, we integrate unique components from the largest state vector into those of smaller dimensions. For example, the component $\hat{m}_2^{(2)}$ specific to $M^{(2)}$ is added to the state vectors of $M^{(0)}$ and $M^{(1)}$. Additionally, where the component \hat{m}_1 exists across multiple models (as in $M^{(1)}$ and $M^{(2)}$), it is averaged to form the augmented component for $M^{(0)}$.

The augmented state vectors and their covariance matrices of $M^{(1)}$ and $M^{(0)}$ are then constructed as follows:

$$\hat{\mathbf{m}}^{(1)} = \begin{bmatrix} \hat{m}_0^{(1)} \\ \hat{m}_1^{(1)} \\ \hat{m}_2^{(2)} \end{bmatrix}, \hat{\mathbf{C}}^{(1)} = \begin{bmatrix} C_0^{(1)} & C_{01}^{(1)} & 0 \\ C_{10}^{(1)} & C_1^{(1)} & 0 \\ 0 & 0 & C_2^{(2)} \end{bmatrix} \quad (43)$$

$$\hat{\mathbf{m}}^{(0)} = \left[\hat{m}_0^{(0)}, \frac{\hat{m}_1^{(1)} + \hat{m}_1^{(2)}}{2}, \hat{m}_2^{(2)} \right]^\top, \quad (44)$$

$$\hat{\mathbf{C}}^{(0)} = \mathbf{diag} \left(C_0^{(0)}, \frac{C_1^{(1)} + C_1^{(2)}}{4}, C_2^{(2)} \right)$$

This approach ensures that each model's state vector in the mixing stage is dimensionally consistent with the most complex model, thereby reducing bias in the IMM's estimations. Note that the augmented components are considered only during the mixing stage. They are excluded from subsequent EKF iterations to maintain focus on the relevant dimensions of each model.

2) *Designing Adaptive Transition Strategies*: The conventional IMM method often struggles to meet performance expectations in dynamic environments due to its reliance on a fixed TPM predicated on prior knowledge. This limitation has spurred researchers to develop methods that enable the TPM to adapt more effectively, not just based on historical data but also incorporating real-time information. We build upon these efforts in our work, especially drawing on the correction functions proposed in [45] and [46]. We leverage these concepts to refine and implement a TPM adjustment mechanism that responds dynamically to current system states, enhancing the IMM's responsiveness and accuracy in diverse operation scenarios.

The first correction function is proposed based on the model probability variation trend. it can be expressed as

$$f_k^{(j)} = \frac{1}{1 - \Delta\mu_k^{(j)}}, \quad (j = 0, 1, \dots, r) \quad (45)$$

$$\Delta\mu_k^{(j)} = \mu_k^{(j)} - \mu_{k-1}^{(j)} \quad (46)$$

where $\Delta\mu_k^{(j)}$ is the gradient of the probability of model j .

The element of TPM is corrected by

$$\bar{p}_{ij}(k) = p_{ij}(k-1)f_k^{(j)}, \quad (i = 0, 1, \dots, r) \quad (47)$$

The first correction function $f_k^{(j)}$ benefits the system when the true model is unchanged. It cannot improve the responsiveness of the IMM method when a model jump happens.

We utilize an activating correction function described in [46] to reduce lag errors and improve the responsiveness of IMM when the model jumps. The activating function is designed as

$$g_k^{(i)} = \frac{1}{1 + \exp\Delta^{(i)}}, \quad (i = 0, 1, \dots, r) \quad (48)$$

$$\Delta^{(i)} = \mu_k^{(i)} - \sum_{j=1, j \neq i}^r \mu_{k-1}^{(j)} \quad (49)$$

where $\Delta^{(i)}$ is the cross-difference model probability from model j to model i at time step $k-1$ and k . It examines the switching between models. Implementing this correction function to p_{ij} can reduce the delay time in the model transition period.

Similar to (47), the corrected term of TPM using $g_k^{(i)}$ is

$$\tilde{p}_{ij}(k) = p_{ij}(k-1)g_k^{(i)}, \quad (i = 0, 1, \dots, r) \quad (50)$$

Combining (47) and (50), we can obtain an integrated term of TPM as

$$\hat{p}_{ij}(k) = \bar{p}_{ij}(k) - \tilde{p}_{ij}(k), \quad (i = 0, 1, \dots, r) \quad (51)$$

$$= p_{ij}(k-1)(f_k^{(j)} - g_k^{(i)})$$

To satisfy the requirement of the Markov chain, the sum of each row of TPM is supposed to equal 1. So, the element of corrected TPM is further normalized as

$$p_{ij}(k) = \frac{\hat{p}_{ij}(k)}{\sum_{j=1}^M \hat{p}_{ij}(k)} \quad (52)$$

Dislike the strategy of using $g_k^{(i)}$ at all time steps in [46], we introduce the minimum likelihood ratio between models as a prior judging condition to know if the current model jumps. The reason is that this correction function may cause instability in cases with large noises and no dominant model. The likelihood ratio is expressed as

$$\lambda_{ij} = \frac{\Lambda_i}{\Lambda_j}, \quad j = [0, 1, \dots, r] \quad (53)$$

where $i \neq j$, Λ_i and Λ_j represent the likelihoods of model i and j .

For the situation with model i being the matched model, it will have the highest likelihood compared to others. Thus, the minimum likelihood ratio $\min[\lambda_{ij}]$ is larger than 1. When model i becomes unmatched, $\min[\lambda_{ij}]$ will largely decrease and be less than 1. So, $\min[\lambda_{ij}]$ can be used as a status indicator to know whether model jumping happens. For model i , We incorporate a model jumping threshold Th_i with $\min[\lambda_{ij}]$ to judge the system status.

Based on the above analysis, the element of corrected TPM can be further updated as

$$\hat{p}_{ij}(k) = \begin{cases} \bar{p}_{ij}(k) - \tilde{p}_{ij}(k), & \min[\lambda_{ij}] \leq \text{Th}_i \\ \bar{p}_{ij}(k), & \min[\lambda_{ij}] > \text{Th}_i \end{cases} \quad (54)$$

C. Proposed Algorithm

We can simplify the strategies for state augmentation and TPM correction to mitigate the risk of overestimation and instability.

By assuming zero covariance on extra components of the augmented state vector, (43) and (44) become

$$\hat{\mathbf{m}}^{(1)} = \begin{bmatrix} \hat{m}_0^{(1)} \\ \hat{m}_1^{(1)} \\ \hat{m}_2^{(2)} \end{bmatrix}, \quad \hat{\mathbf{C}}^{(1)} = \begin{bmatrix} C_0^{(1)} & C_{01}^{(1)} & 0 \\ C_{10}^{(1)} & C_1^{(1)} & 0 \\ 0 & 0 & 0 \end{bmatrix} \quad (55)$$

$$\hat{\mathbf{m}}^{(0)} = \begin{bmatrix} \hat{m}_0^{(0)}, \frac{\hat{m}_1^{(1)} + \hat{m}_1^{(2)}}{2}, \hat{m}_2^{(2)} \end{bmatrix}^\top, \quad (56)$$

$$\hat{\mathbf{C}}^{(0)} = \text{diag}(C_0^{(0)}, 0, 0)$$

By ignoring the second correction function $g_k^{(i)}$, (54) can be simplified as

$$\hat{p}_{ij}(k) = \bar{p}_{ij}(k) \quad (57)$$

Based on theoretical considerations and preliminary analysis, we initially conceptualize two enhanced IMM-EKFs based on these refining strategies.

- **Dual Adaptive IMM-EKF (DAIMM-EKF):** This approach assumes zero covariance for the augmented state vectors using (55) and (56), and employs a dual-correction function (54) for TPM modulation.
- **Single Adaptive IMM-EKF (SAIMM-EKF):** This approach maintains nonzero covariance based on the original state elements for the augmented states using (43) and (44), and uses a single correction function (57) for TPM adjustment.

The entire process of these enhanced IMM-EKFs is detailed in Algorithm 1.

Algorithm 1 Proposed enhanced IMM-EKF method

Input: $\mathcal{D}\{\mathbf{y}_k, \mathbf{u}_k\}$, $k=1, \dots, N$; \mathbf{Q}_v ; \mathbf{R}_n ;

Initialization: $\mathbf{P}_0, \mu_0^{(j)}, \hat{\mathbf{m}}_0^{(j)}, \hat{\mathbf{C}}_0^{(j)}$ $j = [0, 1, \dots, r]$
1: for $k = 1$ **to** N **do**

1) Model interaction:

2: for $i = 0$ **to** r **do**

3: | $\tilde{\mu}_k^{(i)} = \sum_{j=0}^r p_{ji} \mu_{k-1}^{(j)}$

4: | $\mu_{k-1}^{(j)(i)} = \frac{p_{ji} \mu_{k-1}^{(j)}}{\tilde{\mu}_k^{(i)}}$

5: | **Update** $\hat{\mathbf{m}}_{k-1}^j$ **and** $\hat{\mathbf{C}}_{k-1}^{(j)}$ **using** (55), (56) **or** (43), (44)

6: | $\hat{\mathbf{m}}_{k-1}^{(0i)} = \sum_{j=0}^r \mu_{k-1}^{(j)(i)} \hat{\mathbf{m}}_{k-1}^{(j)}$

7: | $\hat{\mathbf{C}}_{k-1}^{(0i)} = \sum_{j=0}^r \mu_{k-1}^{(j)(i)} [\hat{\mathbf{C}}_{k-1}^{(j)} + (\hat{\mathbf{m}}_{k-1}^{(j)} - \hat{\mathbf{m}}_{k-1}^{(0i)})(\hat{\mathbf{m}}_{k-1}^{(j)} - \hat{\mathbf{m}}_{k-1}^{(0i)})^\top]$

8: | end for

2) Shape state estimation with r EKFs:

9: for $i = 0$ **to** r **do**

10: | $\check{\mathbf{m}}_k^{(i)} = \mathbf{f}(\hat{\mathbf{m}}_{k-1}^{(0i)}, \mathbf{u}_k)$

11: | $\check{\mathbf{C}}_k^{(i)} = \mathbf{F}_k^{(i)} \hat{\mathbf{C}}_{k-1}^{(0i)} (\mathbf{F}_k^{(i)})^\top + \mathbf{Q}^{(i)}$

12: | $\mathbf{S}_k^{(i)} = \mathbf{H}_k^{(i)} \check{\mathbf{C}}_k^{(i)} (\mathbf{H}_k^{(i)})^\top + \mathbf{R}^{(i)}$

13: | $\mathbf{K}_k^{(i)} = \check{\mathbf{C}}_k^{(i)} (\mathbf{H}_k^{(i)})^\top (\mathbf{S}_k^{(i)})^{-1}$

14: | $\hat{\mathbf{m}}_k^{(i)} = \check{\mathbf{m}}_k^{(i)} + \mathbf{K}_k^{(i)} (\mathbf{y}_k - \mathbf{h}_p(\check{\mathbf{m}}_k^{(i)}))$

15: | $\hat{\mathbf{C}}_k^{(i)} = (\mathbf{I} - \mathbf{K}_k^{(i)} \mathbf{H}_k^{(i)}) \check{\mathbf{C}}_k^{(i)}$

16: | end for

3) Model likelihood update:

17: for $i = 0$ **to** r **do**

18: | $\Lambda_k^{(i)} = \mathcal{N}(\mathbf{y}_k - \mathbf{h}_p(\hat{\mathbf{m}}_k^{(i)}); \mathbf{0}, \mathbf{S}_k^{(i)})$

19: | $\mu_k^{(i)} = \frac{\tilde{\mu}_k^{(i)} \Lambda_k^{(i)}}{\sum_{j=0}^r \tilde{\mu}_k^{(j)} \Lambda_k^{(j)}}$

20: | end for

4) State estimate combination:

21: | $\hat{\mathbf{m}}_k = \sum_{i=0}^r \mu_k^{(i)} \hat{\mathbf{m}}_k^{(i)}$

22: | $\hat{\mathbf{C}}_k = \sum_{i=0}^r \mu_k^{(i)} (\hat{\mathbf{C}}_k^{(i)} + (\hat{\mathbf{m}}_k - \hat{\mathbf{m}}_k^{(i)})(\hat{\mathbf{m}}_k - \hat{\mathbf{m}}_k^{(i)})^\top)$

5) TPM update:

23: for $i = 0$ **to** r **do**

24: | $\lambda_{ij} = \frac{\Lambda_i}{\Lambda_j}, \quad j = [0, 1, \dots, r], \quad i \neq j$

25: | **Update** \hat{p}_{ij} **using** (54) **or** (57)

26: | $p_{ij} = \frac{\hat{p}_{ij}}{\sum_{j=0}^M \hat{p}_{ij}}$

27: | end for

28: end for

V. OBSERVABILITY ANALYSIS

A. Noise-weighted Observability Matrix

For each model within our Interactive Multiple Model (IMM) framework, we utilize an Extended Kalman Filter

(EKF) to estimate the shape state \mathbf{m} . To ensure the convergence of the EKF, the system must be observable. While observability for linear time-invariant (LTI) systems can be straightforwardly assessed using the observability matrix rank test, determining observability for nonlinear systems is more complex. In our approach, we consider local weak observability, a widely used method for nonlinear systems [47].

A nonlinear system is considered locally weakly observable if the observability rank condition holds in a neighborhood around a specific point in its state space. This condition is constructed using Lie derivatives to form the observability matrix.

The 0^{th} order Lie derivative of output $\mathbf{h}_p(\mathbf{m}_k)$ is itself:

$$(\mathcal{L}_f^0 \mathbf{h}_p)(\mathbf{m}_k, \mathbf{u}_k) = \mathbf{h}_p(\mathbf{m}_k) \quad (58)$$

The 1^{st} order Lie derivative of output $\mathbf{h}_p(\mathbf{m}_k)$ along its vector field $\mathbf{f}(\mathbf{m}_k, \mathbf{u}_k)$ is given by:

$$(\mathcal{L}_f^1 \mathbf{h}_p)(\mathbf{m}_k, \mathbf{u}_k) = \frac{\partial \mathbf{h}_p(\mathbf{m}_k)}{\partial \mathbf{m}_k} \mathbf{f}(\mathbf{m}_k, \mathbf{u}_k) \quad (59)$$

where $\mathbf{f}(\mathbf{m}_k, \mathbf{u}_k) = \dot{\mathbf{m}}(k \cdot T_s)$ and T_s is the sampling time.

The j^{th} order Lie derivative is given by:

$$\left(\mathcal{L}_f^j \mathbf{h}_p \right) (\mathbf{m}_k, \mathbf{u}_k) = \frac{\partial \left(\mathcal{L}_f^{j-1} \mathbf{h}_p \right) (\mathbf{m}_k, \mathbf{u}_k)}{\partial \mathbf{m}_k} \mathbf{f}(\mathbf{m}_k, \mathbf{u}_k) \quad (60)$$

The observability matrix of the shape state is defined as:

$$\mathcal{O}_m(\mathbf{m}_k, \mathbf{u}_k) = \frac{\partial}{\partial \mathbf{m}_k} \begin{bmatrix} \left(\mathcal{L}_f^0 \mathbf{h}_p \right) (\mathbf{m}_k, \mathbf{u}_k) \\ \left(\mathcal{L}_f^1 \mathbf{h}_p \right) (\mathbf{m}_k, \mathbf{u}_k) \\ \vdots \\ \left(\mathcal{L}_f^{n-1} \mathbf{h}_p \right) (\mathbf{m}_k, \mathbf{u}_k) \end{bmatrix} \quad (61)$$

The shape states are locally observable at point $(\mathbf{m}_k, \mathbf{u}_k)$ if and only if the matrix $\mathcal{O}_m(\mathbf{m}_k, \mathbf{u}_k)$ has full rank, i.e., the rank of $\mathcal{O}_m(\mathbf{m}_k, \mathbf{u}_k)$ should be n . To guarantee system observability, the dimension of the estimated states must match the rank of the observability matrix.

The observability matrix is typically used to evaluate the observability of a system for different configurations using the same measurements. However, when assessing observability for the same configuration under varying measurement conditions, traditional methods may not be fully effective. Sensor noise can significantly impact observability evaluations.

To address this issue, we propose a novel approach: the noise-weighted observability matrix. This method accounts for the impact of sensor noise on observability by incorporating noise levels directly into the observability assessment. The noise-weighted observability matrix is defined as:

$$\mathcal{O}_{\mathbf{wm}} = \mathcal{O}_m^\top \mathbf{R}^{-1} \mathcal{O}_m \quad (62)$$

B. Assesment of observability

1) *Inverse condition number*: In practical applications, where measurements and inputs are noisy, relying solely on a rank test for local observability is often impractical. Instead, the inverse condition number is commonly used as a metric for observability. It is defined as:

$$inv_cond(\mathcal{O}_{\mathbf{wm}}) = \frac{\sigma_{\min}(\mathcal{O}_{\mathbf{wm}})}{\sigma_{\max}(\mathcal{O}_{\mathbf{wm}})} \quad (63)$$

where σ_{\max} and σ_{\min} denote the maximum and minimum singular values of $\mathcal{O}_{\mathbf{wm}}$, respectively. A matrix approaching rank deficiency will have an inverse condition number approaching zero. Generally, a value closer to 1 indicates better observability. However, this index is dimensionless and may not always distinguish between different levels of observability effectively [48].

2) *Noise amplification index*: To address the limitations of the inverse condition number, we also introduce the noise amplification index, as proposed in [48]. It is defined as:

$$noise_amp(\mathcal{O}_{\mathbf{wm}}) = \frac{\sigma_{\min}^2(\mathcal{O}_{\mathbf{wm}})}{\sigma_{\max}(\mathcal{O}_{\mathbf{wm}})} \quad (64)$$

This index measures how noise impacts observability. A higher value indicates better observability, complementing the inverse condition number by offering a more nuanced view of the system's performance.

VI. SIMULATION STUDY

To evaluate the feasibility and performance of the proposed shape estimation method, we conduct simulation studies programmed in *Python* environment. Firstly, we analyze the impact of sensor arrangement on the shape estimation by using a standard EKF with $M^{(2)}$. Then, we choose the optimal sensor arrangement to evaluate the proposed IMM-EKF algorithms.

A. Data generation

1) *Ground truth shapes and modal coefficients*: We simulate a bending process ranging from a nearly straight configuration to a significantly bent configuration. This process is represented through a sequence of 100 samples, employing three distinct models within our model set \mathbb{M} . The simulations focus on the central backbone of the continuum robot, with a fixed length $L = 100mm$. Each simulation step corresponds to a sampling time $T_s = 1s$, driven by a constant system input defined as the velocity of bending angle at the tip $\dot{\theta}_e = 0.02517rad/s$. This approach generates a comprehensive set of simulated ground truth shapes alongside their corresponding modal coefficients, as depicted in Fig. 6.

2) *Measurements*: For the measurements in different sensor arrangements, we extract position and orientation at specified arc lengths based on the ground truth of modal coefficients generated previously and introduce noise to them to emulate real sensor behavior. This noise is generated by drawing random values from a zero-mean Gaussian distribution, with standard deviations set to reflect typical sensor inaccuracies

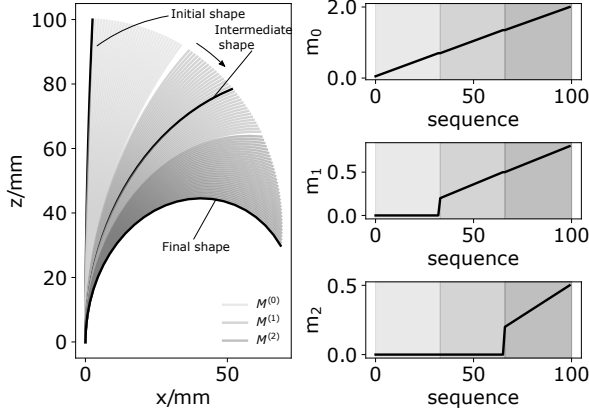


Fig. 6: Simulation ground truth shapes and modal coefficients across different polynomial stages. The figure shows ground truth shapes (left) and modal coefficients m_0 , m_1 and m_2 (right) across three stages of the simulation, each defined by a different polynomial curvature model: $M^{(0)}$ for Stage I, $M^{(1)}$ for Stage II, and $M^{(2)}$ for Stage III. The modal coefficients directly determine the shapes at each stage, as indicated by the shaded background corresponding to each polynomial order.

encountered in practice. Specifically, we set the standard deviation for position measurement at $\nu_r = 1.5\text{mm}$ and for orientation measurements at $\nu_\psi = 1.72^\circ$.

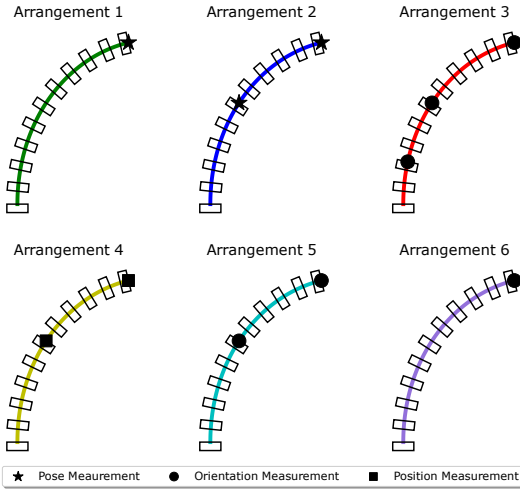


Fig. 7: Sensor arrangement configurations for simulation measurements on a continuum robot. Arrangement 1 has a single pose sensor at the tip ($s=1$); Arrangement 2 has two pose sensors at $s=1$ and $s=0.5$; Arrangement 3 places three orientation sensors at $s=1$, $s=0.5$, and $s=0.2$; Arrangement 4 positions two position sensors at $s=1$ and $s=0.5$; Arrangement 5 includes two orientation sensors at $s=1$ and $s=0.5$; Arrangement 6 features a single orientation sensor at the tip.

B. Sensor arrangement evaluation

1) *Sensor setup*: We investigate six distinct sensor arrangements to assess their advantages and constraints in constructing the shape of a continuum robot. These arrangements are detailed in Fig. 7, where we illustrate the configurations using six sample shapes.

2) *Estimator settings*: In this simulation study, we employ model $M^{(2)}$, characterized by a 2^{nd} order polynomial curvature function, in conjunction with the EKF to assess the influence of different sensor arrangements on shape estimation accuracy. The state vector is $\mathbf{m}^{(2)} = [m_0^{(2)}, m_1^{(2)}, m_2^{(2)}]^\top$.

For the EKF setup tailored to our shape estimation task, the process noise covariance matrix, denoted as \mathbf{Q} , underwent empirical tuning to optimize the estimator's performance, ensuring it effectively balances sensitivity to model dynamics and measurement noise.

The dimensionality of the measurement noise covariance matrix \mathbf{R} is contingent upon the specific sensor arrangement employed. It is structured as a diagonal matrix where the position-related terms are set to $10\nu_r^2$ and the orientation-related terms to $10\nu_\psi^2$, reflecting our estimation of the measurement uncertainties associated with position and orientation sensors, respectively.

3) *Evaluation metrics*: In evaluating the performance of estimators, we utilize two methodologies: error analysis in Cartesian space and error analysis in modal coefficient space.

For the Cartesian space, we consider the absolute position and rotation errors at the robot's tip ($e_{p_{tip}}$, $e_{r_{tip}}$) and root mean square error (RMSE) at multiple even-distributed locations along the arc length ($e_{p_{shape}}$, $e_{r_{shape}}$).

The absolute position error at the robot's tip, denoted as $e_{p_{tip}}$, is calculated as the Euclidean distance between the estimated position and the ground truth position in the Cartesian plane:

$$e_{p_{tip}} = |p_{est} - p_g| = \sqrt{(x_{est} - x_g)^2 + (z_{est} - z_g)^2} \quad (65)$$

where $p_{est} = (x_{est}, z_{est})$ represents the estimated position of the robot's tip, $p_g = (x_g, z_g)$ represents the ground truth position.

The rotation error at the robot's tip, denoted as $e_{r_{tip}}$, is defined as the absolute difference between the estimated and the ground truth bending angles:

$$e_{r_{tip}} = |\theta_{est} - \theta_g| \quad (66)$$

where θ_{est} and θ_g represent the estimated and ground truth bending angle, respectively.

The corresponding shape errors for the robot are defined as the root mean square errors (RMSE) for both position and rotation along the arc length. These errors include data from all indexed disks as follows:

For position:

$$e_{p_{shape}} = \sqrt{\frac{1}{n} \sum_{i=0}^{n-1} (p_{est,i} - p_{g,i})^2}, \quad (67)$$

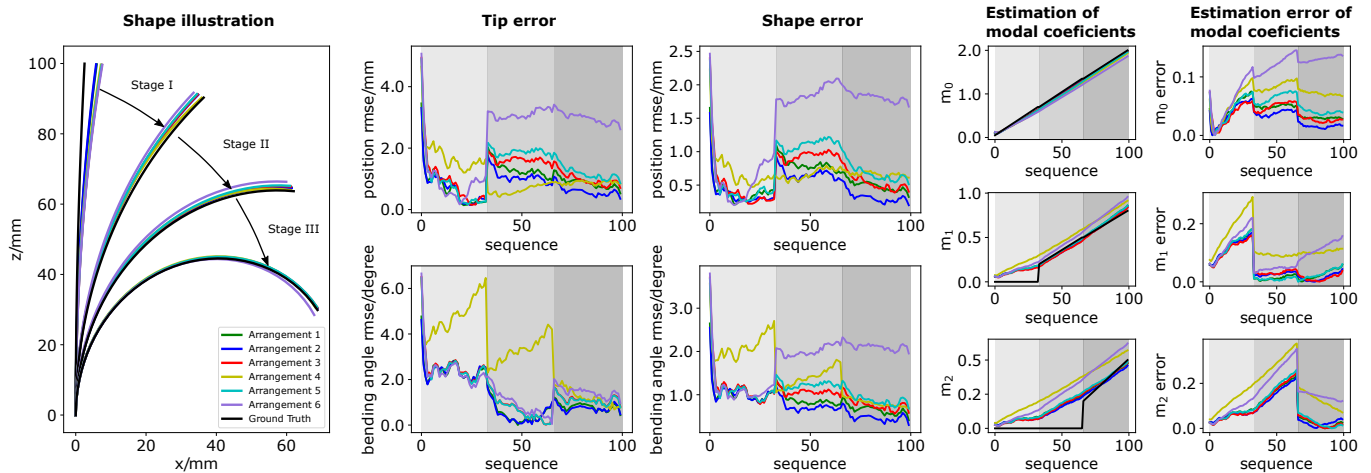


Fig. 8: Estimation performance of different sensor arrangements using a standard EKF with $M^{(2)}$. The leftmost panel shows shape illustrations at three stages of the simulation, with the actual shape denoted as ‘Ground Truth’. The subsequent panels detail the tip error, shape error, and the estimation and error of modal coefficients (m_0 , m_1 , m_2) across the sequence. Shaded areas in the error panels indicate different simulation stages defined in fig. 6.

where $p_{est,i}$ and $p_{g,i}$ are the estimated and ground truth positions at i^{th} disk. Indices range from $i = 0$, corresponding to the disk at the robot’s tip, to $i = n - 1$, which refers to the first disk immediately above the base. The total number of disks evaluated is $n = 10$.

For rotation:

$$e_{r_{shape}} = \sqrt{\frac{1}{n} \sum_{i=0}^{n-1} (\theta_{est,i} - \theta_{g,i})^2}, \quad (68)$$

where $\theta_{est,i}$ and $\theta_{g,i}$ are the estimated and ground truth bending angles at i^{th} disk.

In modal coefficient space, we focus on the absolute error of the modal components of the shape state vector. This approach allows us to assess the accuracy of our shape representation in terms of its modal characteristics. Combining these two metrics offers a comprehensive evaluation of the estimation performance, capturing both spatial accuracy and the fidelity of the novel shape state representation using modal coefficients.

In addition, we investigate the observability of each sensor arrangement using indices described in section V-B.

4) *Results:* The estimation results across six sensor arrangements in Cartesian space are illustrated in fig. 8. The right plots display the estimation results of the shape state (modal coefficients). The tip error and shape error in both position and orientation are illustrated in the middle plots. The left plot shows the ground truth and the estimated shapes at four sample points.

We analyze the estimation results based on the observability of each arrangement. When we examine the rank condition of the observability matrix for each sensor arrangement, it becomes apparent that the observability matrices for arrangements 5 and 6 are not full rank, indicating that these scenarios are not observable. In contrast, the other four arrangements appear to be observable.

As unobservable scenarios, Arrangements 5 and 6 exhibit acceptable performance in Stage I, showing low errors in tip position and bending angles, similar to observable arrangements. However, these arrangements show distinct divergence in tip position and shape errors in Stages II and III, particularly for Arrangement 6. Despite these challenges, the bending angle errors at the tip remain consistently low across all stages for both arrangements. This stability is attributed to using orientation measurements in the estimations, which effectively maintain accuracy in the bending angle despite other increasing errors.

For the observable arrangements, most exhibit small tip and shape errors in both position and orientation across all stages, except for Arrangement 4, which utilizes two position measurements. In Arrangement 4, although position errors are relatively low, the orientation errors are considerably larger, particularly in Stages I and II. To further assess their observability, we evaluated two indices—the inverse condition number and the noise amplification index—of both the conventional observability matrix \mathcal{O}_m and the noise-weighted observability matrix \mathcal{O}_{wm} . The results, depicted in Fig. 11, show conventional observability indices on the left and noise-weighted indices on the right. Unlike the indices from the conventional observability matrix, which show no correlation with the estimation results, the indices from the noise-weighted matrix demonstrate a clear correlation between observability and estimation accuracy of the modal coefficients. The estimation results for the shape states (modal coefficients) are consistent with the pose estimations at the tip and the overall shape. The average values of all evaluation metrics, calculated over 100 sample shapes, are presented in Table III. Arrangement 2 exhibits the best performance, with the lowest average errors: 0.80 mm for tip position, 0.45 mm for shape position error, 1.21 degrees for tip bending angle, and 0.76 degrees for shape bending angle error. Furthermore,

TABLE III: Estimation errors of sensor arrangement evaluation

| Arrangement | 1 | 2 | 3 | 4 | 5 | 6 |
|---|------|-------------|-------------|-------|------|-------|
| Position (Mean)/mm | | | | | | |
| Tip Abs. Error | 0.96 | 0.80 | 1.19 | 1.09 | 1.31 | 2.37 |
| Shape RMSE | 0.57 | 0.45 | 0.65 | 0.68 | 0.76 | 1.44 |
| Bending angle (Mean)/deg | | | | | | |
| Tip Abs. Error | 1.23 | 1.21 | 1.47 | 3.10 | 1.45 | 1.61 |
| Shape RMSE | 0.87 | 0.76 | 1.01 | 1.45 | 1.10 | 1.78 |
| Modal coefficient (Mean)/10 ⁻² | | | | | | |
| m_0 Abs. Error | 4.05 | 3.04 | 3.73 | 6.92 | 4.94 | 10.34 |
| m_1 Abs. Error | 5.32 | 5.30 | 5.16 | 12.60 | 5.27 | 9.86 |
| m_2 Abs. Error | 8.08 | 7.51 | 7.81 | 17.56 | 8.56 | 15.44 |

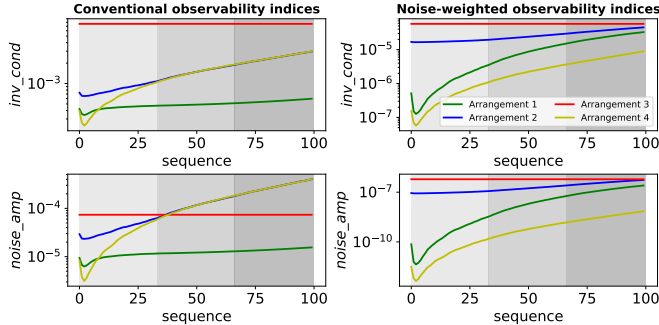


Fig. 9: Observability assessment through inverse condition number and noise amplification index. The upper graph shows the inverse condition numbers, while the lower graph presents the noise amplification indices for observable arrangements. Shaded regions indicate Stages I, II, and III, respectively.

Arrangement 2 also achieves the smallest errors in estimating modal coefficients.

C. IMM-EKF Evaluation

This section compares the performances of our proposed IMM-EKF algorithms - DAImm-EKF and SAImm-EKF - against the conventional IMM-EKF (CIMM-EKF) and the standard EKF with $M^{(2)}$ under Arrangement 2.

1) *Estimator settings*: We use the same EKF settings of sensor arrangement evaluation for elementary EKFs of the IMM-EKF evaluation. As for IMM, we initialize TPM as follow, assuming no prior knowledge:

$$\mathbf{P} = \begin{bmatrix} 0.7 & 0.15 & 0.15 \\ 0.15 & 0.7 & 0.15 \\ 0.15 & 0.15 & 0.7 \end{bmatrix} \quad (69)$$

The initialized model probability is set as

$$\mu_0^i = \frac{1}{3}, \quad i = [0, 1, \dots, r] \quad (70)$$

Specifically, one more step needs to be considered for the DAImm-EKF - setting up the likelihood ratio threshold Th_i . Through our empirical tuning, the estimator yields enhanced performance when setting thresholds as follows $\text{Th}_0 = 1.2$, $\text{Th}_1 = 0.75$, $\text{Th}_2 = 0.75$.

TABLE IV: Estimation errors of IMM-EKF evaluation

| Estimator | EKF($M^{(2)}$) | CIMM | DAImm | SAImm |
|--|------------------|-------|-------------|-------|
| Position (Mean)/mm | | | | |
| Tip Abs. Error | 0.80 | 0.89 | 0.44 | 0.51 |
| Shape RMSE | 0.45 | 0.62 | 0.24 | 0.31 |
| Bending angle (Mean)/deg | | | | |
| Tip Abs. Error | 1.21 | 1.59 | 0.69 | 0.83 |
| Shape RMSE | 0.76 | 0.94 | 0.40 | 0.50 |
| Modal components (Mean)/10 ⁻² | | | | |
| m_0 Abs. Error | 3.04 | 6.55 | 1.64 | 2.63 |
| m_1 Abs. Error | 5.30 | 12.72 | 3.90 | 5.51 |
| m_2 Abs. Error | 7.51 | 8.73 | 3.76 | 5.18 |

2) *Results*: The pose errors for the four estimators are displayed in Fig. 10. Again, shape errors follow the trends observed in tip errors but with reduced magnitudes. The standard EKF exhibits a smoother error profile compared to the IMM variants. In Stage I, IMM estimators surpass the elementary EKF in accuracy, particularly evident in bending angle errors at the tip. Upon transitioning to a more complex model, CIMM-EKF's performance dips due to its unchanging TPM and dimensional bias issues. In contrast, DAImm-EKF and SAImm-EKF demonstrate superior error reduction, outperforming the standard EKF.

The right plots of fig. 10 illustrated the errors of modal coefficients, clearly highlighting the distinctions between the elementary EKF and IMM-EKF estimators. The elementary EKF excels when its model aligns with the true system model, showing optimal estimation accuracy. However, its performance significantly declines in scenarios with a mismatch between the utilized and true models. Conversely, the IMM-EKF estimators consistently yield better results when dealing with true models of smaller dimensionality. Across all three IMM estimators, the estimation of m_0 is comparably effective. Yet, for m_1 and m_2 , DAImm-EKF outperforms SAImm-EKF, while CIMM-EKF lags, exhibiting the least favorable estimation accuracy.

The average errors for all estimation metrics are presented in tab. IV. DAImm-EKF demonstrates superior performance, recording the lowest average errors: 0.44 mm for position tip, 0.24 mm for shape error in position, 0.69 degrees for bending angle at the tip, and 0.40 degrees for shape error in bending angle. In terms of qualitative performance, both DAImm-EKF and SAImm-EKF surpass the standard EKF in accuracy, while CIMM-EKF falls short.

Figure 11 showcases the model probabilities for CIMM, DAImm, and SAImm, aligned with the sequential use of $M^{(0)}$, $M^{(1)}$, and $M^{(2)}$ in generating the ground truth data. A higher model probability for $M^{(i)}$ indicates closer alignment with the true model, enhancing IMM estimation accuracy. The trendline for CIMM exhibits slow adjustments to model transitions, reflecting the delayed response to changes in the true model.

To address this, DAImm introduces dual correction functions targeting model probability and likelihood ratio alongside

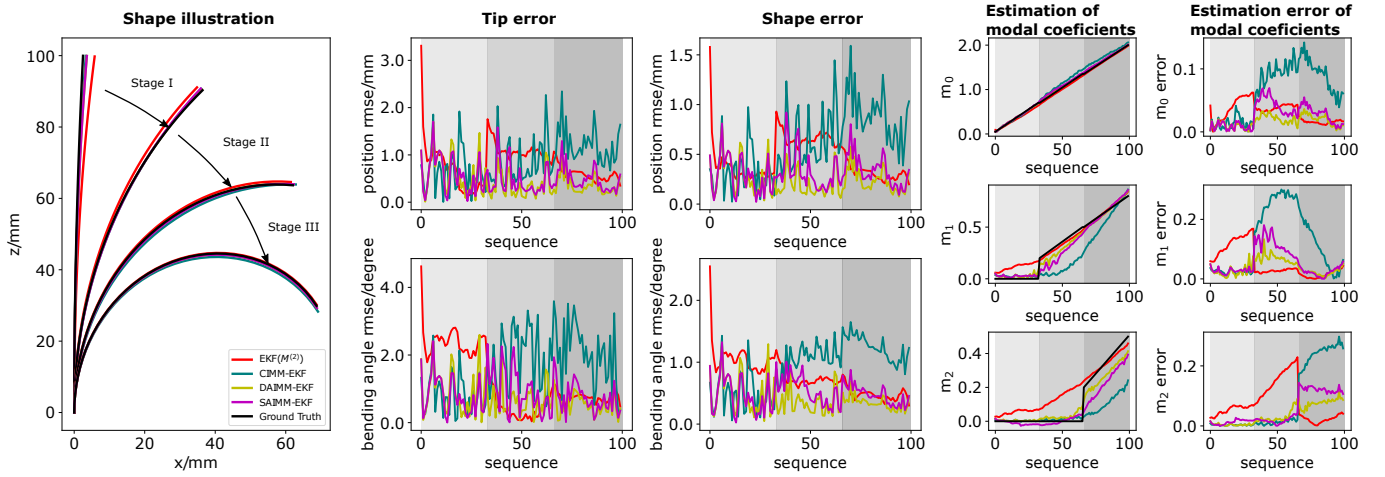


Fig. 10: Comparative performance of proposed DIMM-EKF, SAIMM-EKF, CIMM-EKF and elementary EKF with $M^{(2)}$ under sensor arrangement 2. The left panel illustrates the robot's shape at key sample points against the ground truth. Middle panels quantify tip and shape errors in position and orientation. Right panels display estimation results and their errors for modal coefficients m_0 , m_1 , m_2 .

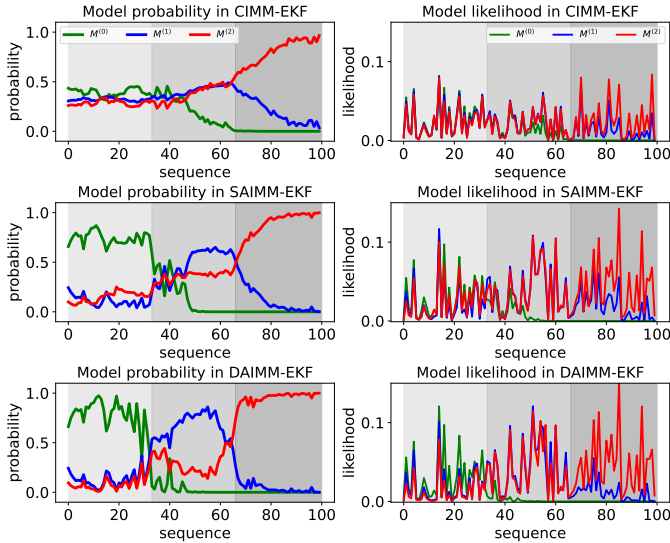


Fig. 11: Model probabilities and likelihoods of IMM-EKF estimators. Each panel shows the probabilities/likelihoods for $M^{(0)}$ (green), $M^{(1)}$ (blue), and $M^{(2)}$ (red) across 100 sequences, highlighting how each estimator adapts its model preference over time.

a straightforward approach to mitigating dimensional bias. SAIMM, on the other hand, employs a single correction function focused on model probability and a more intricate method for dimensional bias correction. Both DAIMM and SAIMM demonstrate quicker adaptation to model transitions, with DAIMM responding more rapidly than SAIMM, significantly reducing lag errors. This rapid response capability contributes to DAIMM's superior estimation performance.

A key challenge with DAIMM is fine-tuning the threshold for the minimum likelihood ratio, which triggers the second correction function. Fig. 11 shows how model likelihoods

behave under DAIMM. Initially, when $M^{(0)}$ is the true model, all three models have similar likelihoods, with $M^{(0)}$ slightly higher. When the model transitions to $M^{(1)}$, the likelihood of $M^{(0)}$ drops sharply, while $M^{(1)}$ and $M^{(2)}$ have comparable likelihoods. If $M^{(2)}$ is the true model, its likelihood clearly exceeds that of the other models. However, distinguishing between models is difficult when the true model has lower dimensionality, due to similar likelihoods. To address this, we use model-specific thresholds for the minimum likelihood ratio, customized for each model's characteristics.

VII. EXPERIMENTAL VALIDATION

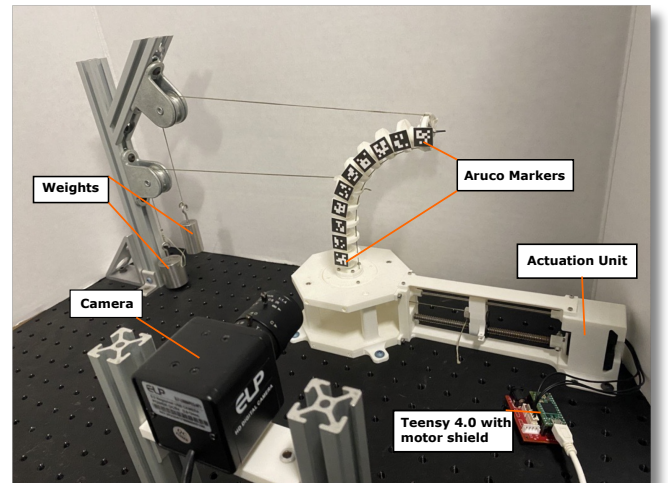


Fig. 12: Experimental setup including the cable-driven continuum robot prototype, camera system and weights.

In this section, we validate the proposed estimation algorithms experimentally using the developed cable-driven continuum robot prototype, as shown in Fig. 12. The prototype

consists of a central backbone made from super-elastic NiTi wire, with a diameter of 1.524 mm and an arc length of 200 mm. Ten evenly distributed 3D-printed spacer disks are assembled to guide four pulling wires. Actuation is achieved using lead-screw mechanism modules driven by servo motors (Dynamixel XL-430, Robotis Inc.). Control commands are managed by a Teensy 4.0 board microcontroller, which is paired with a customized drive shield. The robot design accommodates up to four pulling wires for actuation, each connected to an individual actuation module. For the experimental tests, only one actuation module was used to enable a single, straightforward bending process.

A. Sensor Arrangement

To accurately reconstruct the ground truth shape of the continuum robot during bending, we used Aruco Markers and a USB camera to capture poses along the arc length. Ten markers are affixed at the front of each disk, with each marker’s transformation to the corresponding Frames $\{Gs\}$ pre-defined. Additionally, an Aruco marker was placed at the instrument’s base before the test began, facilitating the computation of the transformation from the camera frame to the robot’s base frame. Given the presence of noise and outliers in Aruco marker detection, a Gaussian smoother was applied to all pose data to establish a reliable ground truth. We selected the raw pose data from the Aruco marker at the tip to evaluate our estimation algorithms. This decision was based on our simulation studies, which showed similar estimation trends across different sensor arrangements. Using just this single sensor arrangement, we aim to provide a focused comparison with conventional estimators, highlighting the effectiveness of our proposed methods under practical conditions.

B. Data Collection and Processing

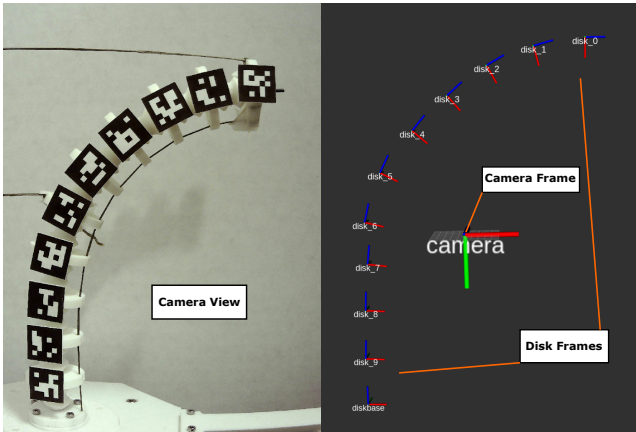


Fig. 13: Experimental data collection. Left: Camera view showing the setup during data capture. Right: Disk frames constructed from Aruco marker pose measurements in the camera frame.

The experimental validation employed four distinct dynamical configurations, each subjected to identical bending processes under varying loading conditions. These configurations

and their setups are depicted in the left figure of Fig 14. Following our simulation methods, changes in the bending angle were converted into motor commands to actuate the wire consistently using inverse kinematics of *joint-to-configuration* space, as detailed in Appendix A. During each scenario, we collected raw pose data from all Aruco markers throughout the bending process within a ROS2 environment [49], enabling us to compute disk poses relative to the base frame. Since our study focuses solely on in-plane bending, determining the bending plane was essential. We collected all y-axes from the Frames $\{Gs\}$ on the disks and employed Singular Value Decomposition (SVD) to pinpoint the principal y-axis. This axis helped establish the normal to the bending plane. Using this principal y-axis alongside the origin of the base frame, we defined the bending plane, enabling the projection of the 6 DOF pose data into 3 DOF within this plane. The projected poses from the Aruco marker at the tip served as the measurement data for our analyses.

C. Results

In the experimental scenarios involving the four bending processes of the continuum robot prototype, we deployed three elementary Extended Kalman Filters (EKF) with $M^{(0)}$, $M^{(1)}$ and $M^{(2)}$, alongside two proposed Interactive Multiple Model EKFs (IMM-EKFs)—DAIMM-EKF and SAIMM-EKF. It was observed that $M^{(0)}$ did not fit well with complex loading configurations, leading to its exclusion from the IMM interaction analysis. Consequently, the model set was redefined as $\mathbb{M} = \{M^{(1)}, M^{(2)}\}$ for evaluating IMM interaction in these tests. The parameter settings for these models were consistent with those used in our simulations.

1) *Pose and shape estimation*: The outcomes of pose estimation and shape illustrations are presented in Fig. 14. SAIMM-EKF stands out as the best performer, achieving the smallest estimation errors among all estimators. DAIMM-EKF, while outperforming elementary EKFs with $M^{(0)}$ and $M^{(1)}$, aligns closely in performance with the EKF with $M^{(2)}$. This alignment is due to DAIMM-EKF’s rapid adaptation, which, after initial mixing stages, leads to a predominant reliance on the $M^{(2)}$. The estimated poses of the continuum robot, depicted in the figures, are calculated from the estimated shape states. The performance hierarchy among the remaining estimators follows as EKF($M^{(2)}$), EKF($M^{(1)}$), and EKF($M^{(0)}$), with EKF($M^{(0)}$) notably underperforming.

The estimation performance of the proposed algorithms, particularly SAIMM-EKF, consistently outperforms the elementary EKFs, demonstrating robustness across four different dynamical configurations. The small estimation errors maintained across these scenarios—some of which include abrupt force applications—further validate the robustness of the algorithms, proving their efficacy in handling complex dynamic challenges.

The modal coefficient results are depicted in the right plots of Fig. 14. Although the ground truth for these coefficients is unverifiable, the estimated modal coefficients from these estimators can be observed. Except for the EKF using $M^{(0)}$,

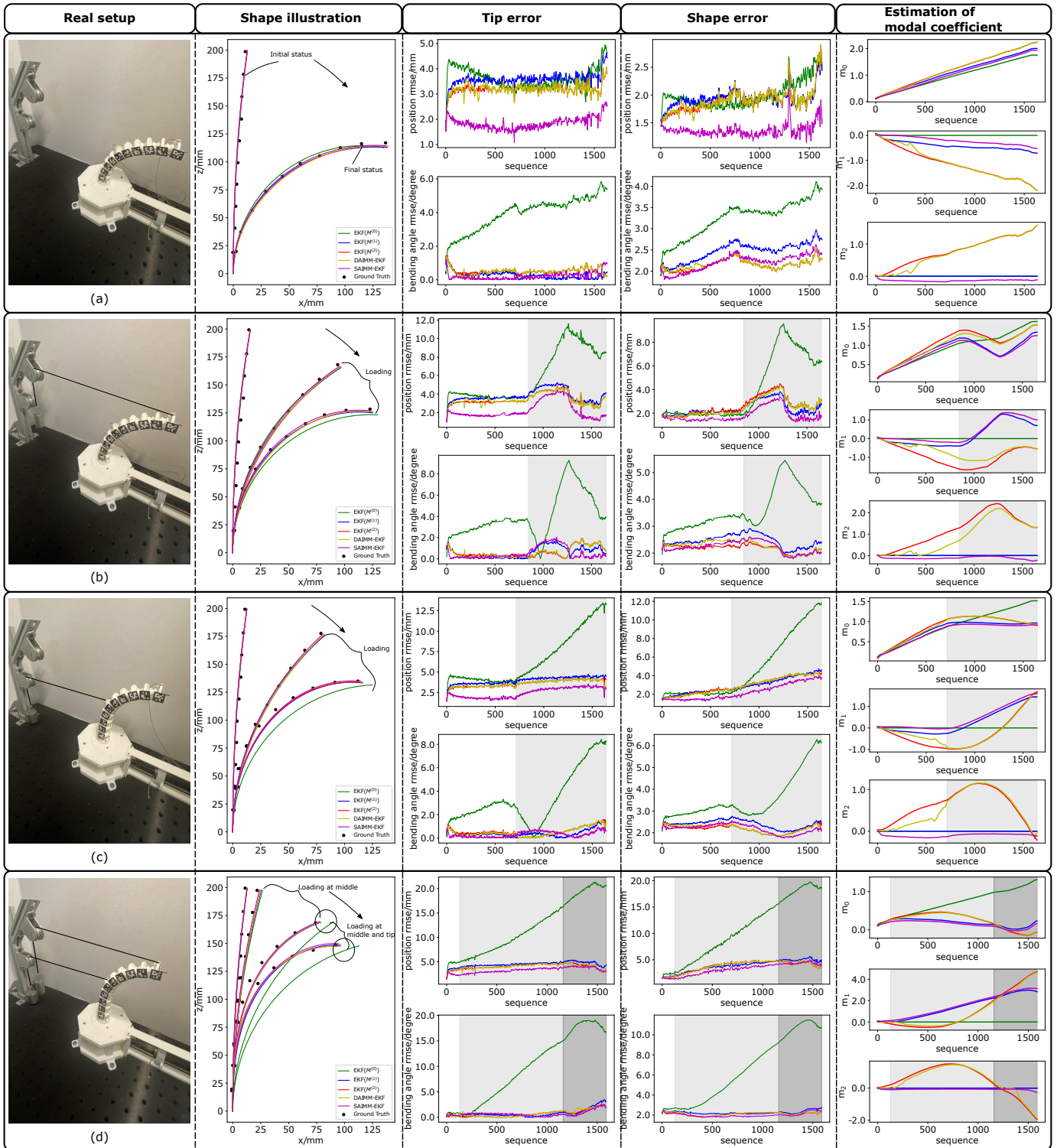


Fig. 14: Comprehensive evaluation of estimation techniques across dynamical scenarios with different loading conditions. Each row represents a dynamic scenario: (a) unloaded, (b) transitioning to tip loading, (c) transitioning to middle loading, and (d) transitioning from middle to combined middle and tip loading. The estimators include three elementary EKF with $M^{(0)}$, $M^{(1)}$, $M^{(2)}$ and two proposed estimators: DAIMM-EKF and SAIMM-EKF. From left to right, the columns display the real setup, shape illustration, tip error over sequences, shape error over sequences, and modal coefficient estimations. Background shading in the error and estimation of modal coefficients plots indicates loading periods, using light grey for single-point loading and darker grey for dual-point loading.

the estimations by the EKF using $M^{(1)}$ in conjunction with SAIMM-EKF, and the EKF using $M^{(2)}$ paired with DAIMM-EKF, display similar trends. Given the superior estimation accuracy of SAIMM-EKF, it is plausible that the true modal coefficients are closer to the results obtained between the estimates from the EKF using $M^{(1)}$ and the EKF using $M^{(2)}$.

2) *Comparison of IMM-EKFs*: Unlike the simulation results, SAIMM-EKF outperforms DAIMM-EKF in real experiments. Observations from Fig. 15, which shows the probability/likelihood of each model, reveal distinct characteristics for each estimator. DAIMM-EKF responds quickly and is capable of amplifying the distinctions between different models. Conversely, SAIMM-EKF is more stable for subtle variations in loading conditions within the dynamic configurations. The reason DAIMM-EKF did not surpass SAIMM-EKF in performance is due to the absence of significant model jumps, regardless of the variations in loading forces applied to the continuum segment. This observation highlights that while DAIMM-EKF excels in scenarios with clear model transitions, SAIMM-EKF provides superior performance in more stable or gradually changing conditions.

VIII. CONCLUSION

In this paper, we proposed a stochastic observer-based shape estimation framework for continuum robots within a polynomial curvature shape state space. We developed two enhanced Interacting Multiple Models coupled with Extended Kalman Filters (IMM-EKFs) to achieve robust shape estimation for dynamic configurations under various loading conditions. These algorithms were tested using limited discrete sensors as measurements, which may include poses, positions, or orientations along the arclength. Additionally, we introduced a noise-weighted observability matrix as an auxiliary tool to optimize sensor arrangement by mitigating noise impact, using an elementary EKF as the baseline. Subsequently, we conducted comprehensive simulations and hardware experiments to evaluate the performance of the two proposed IMM-EKFs: SAIMM-EKF and DAIMM-EKF. The results demonstrated that DAIMM-EKF excels in scenarios where the underlying model undergoes abrupt changes, as shown in simulations, while SAIMM-EKF performs better in real-world conditions where diverse loading scenarios are encountered during the bending process of a cable-driven continuum robot, as validated by experimental results.

The proposed approach can be easily extended to shape estimation for multiple continuum segments. However, a limitation of the current model is that it does not account for torsional effects in the polynomial curvature kinematics. Future work could focus on addressing this by extending the polynomial curvature kinematics into $SE(3)$, incorporating curvature polynomials along all three axes. Additionally, future research could explore the integration of more advanced control algorithms, applying more sophisticated estimation techniques such as Unscented Kalman Filters(UKF) and combining basic static models for force and moment estimation.

APPENDIX

A. Inverse kinematics of joint-to-configuration space

Figure 16 illustrates the inverse kinematics of *joint-to-configuration* space for a continuum segment actuated by four pulling wires. we use $\mathbf{L} = [L_1, L_2, L_3, L_4]^T$ to represent the pulling wire lengths. Similar to the derivation of the position vector $\mathbf{p}(s)$, referring to Fig 16, the length of i^{th} pulling wire L_i can be expressed as:

$$L_i = \int_0^L \left\| \frac{d\mathbf{r}(s)}{dl} \right\| dl = \int_0^L \left\| \frac{d\mathbf{r}(s)}{d(sL)} \right\| d(sL) = \int_0^1 \left\| \frac{d\mathbf{r}(s)}{ds} \right\| ds \quad (71)$$

where $\frac{d\mathbf{r}(s)}{ds} = \frac{d\mathbf{p}(s)}{ds} + \frac{d\mathbf{v}(s)}{ds}$.

$\frac{d\mathbf{p}(s)}{ds}$ can be easily obtained by equation 8. Referring to Fig. 16, $\frac{d\mathbf{v}}{ds}$ is derived as:

$$\frac{d\mathbf{v}}{dl} = \frac{d\mathbf{v}}{d(sL)} = {}^1\mathbf{R}_{e_s} ({}^{e_s}\boldsymbol{\omega}_{g_s} \times {}^{e_s}\mathbf{v}) \quad (72)$$

$${}^{e_s}\boldsymbol{\omega}_{g_s} = \hat{\mathbf{y}} \frac{d\theta(s)}{ds} = [0, \kappa(s), 0]^T \quad (73)$$

$${}^1\mathbf{R}_{e_s} = e^{\theta(s)[\mathbf{e}_2^\wedge]}, {}^{e_s}\mathbf{v} = r [\cos(\sigma_i), \sin(\sigma_i), 0]^T \quad (74)$$

where $\sigma_i(s)$ is the angular coordinate of i^{th} pulling wire with respect to Frame {Es}, which is given by:

$$\sigma_i = \delta_0 + (i - 1)\beta \quad (75)$$

and r designates the constant distance between the central backbone and pulling wires.

Then we can get the length of i^{th} pulling wire L_i by substituting equation 8 and 72 into equation 71 as follows:

$$L_i = \int_0^1 \|L - r\kappa(s)\cos(\sigma_i)\| ds = L - \theta_e r \cos(\sigma_i) \quad (76)$$

The *joint* vector space $\mathbf{q} = [q_1, q_2, q_3, q_4]$, representing the pulling/release displacement of the pulling wires, can be calculated based on equation 76, i.e., $q_i = L_i - L$. Then we define the *joint to configuration* space Jacobian $\mathbf{J}_{\mathbf{q}\psi}$ as the Jacobian relating infinitesimal $\delta\mathbf{q}$ to $\delta\psi$. It can be represented by

$$\mathbf{J}_{\mathbf{q}\psi} = \frac{\partial\mathbf{q}}{\partial\psi} \quad (77)$$

where $\mathbf{J}_{\mathbf{q}\psi}$ will be utilized to establish *joint* space commands based on the control inputs in *configuration* space during experiments.

B. Mixing probability transitioning from model j to i

$$\begin{aligned} \mu_{k-1}^{(j)|(i)} &= P\left(M_{k-1}^{(j)} \mid M_k^{(i)}, \mathbf{y}_{1:k-1}\right) \\ &= \frac{P\left(M_k^{(i)} \mid M_{k-1}^{(j)}, \mathbf{y}_{1:k-1}\right) P\left(M_{k-1}^{(j)} \mid \mathbf{y}_{1:k-1}\right)}{P\left(M_k^{(i)} \mid \mathbf{y}_{1:k-1}\right)} \\ &= \frac{p_{ji}\mu_{k-1}^{(j)}}{\check{\mu}_k^{(i)}} \end{aligned} \quad (78)$$

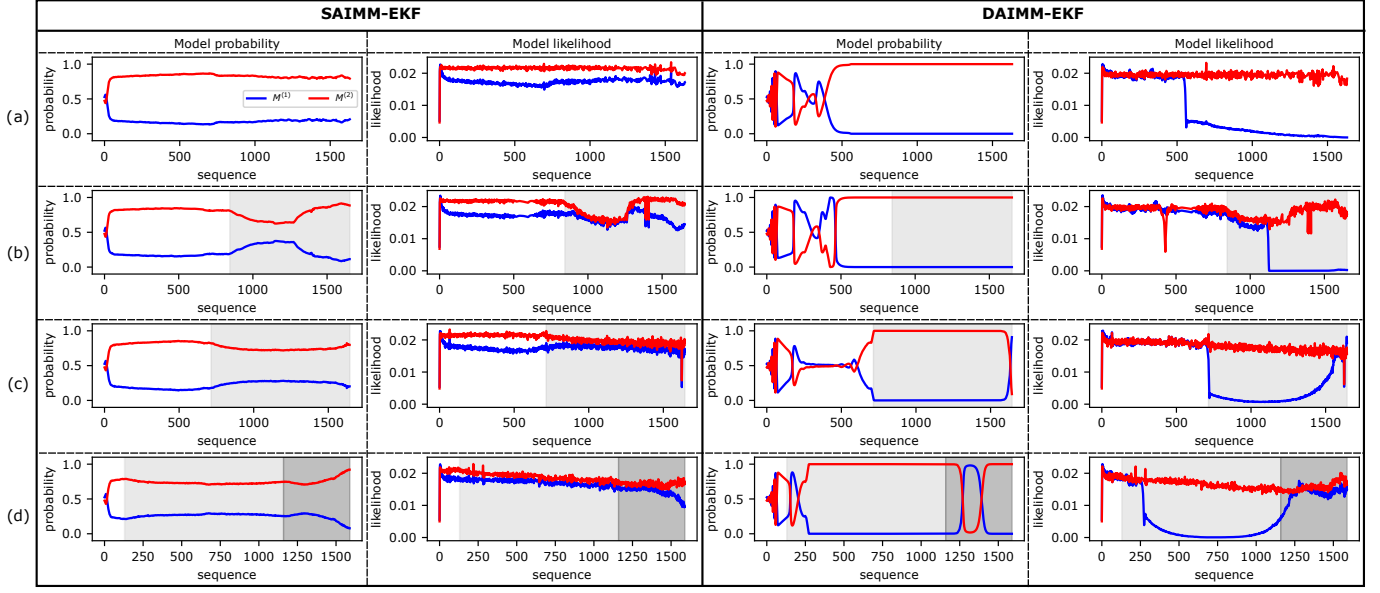


Fig. 15: Model probabilities/likelihoods for DAIMM-EKF and SAIMM-EKF under four dynamical scenarios. (a) unloaded, (b) transitioning to tip loading, (c) transitioning to middle loading, and (d) transitioning from middle to combined middle and tip loading. Red and blue lines indicate the probabilities/likelihoods of $M^{(1)}$ and $M^{(2)}$, respectively. Shaded regions in each subplot reflect the loading phases.

where

$$\check{\mu}_k^{(i)} = P\left(M_k^{(i)} \mid \mathbf{y}_{1:k-1}\right) = \sum_{j=0}^r p_{ji} \mu_{k-1}^{(j)} \quad (79)$$

C. Likelihood and probability update of model i

Updated likelihood of model i :

$$\begin{aligned} \Lambda_k^{(i)} &= \mathcal{N}\left(\mathbf{y}_k - \mathbf{h}_p\left(\check{\mathbf{m}}_k^{(i)}\right); \mathbf{0}, \mathbf{S}_k^{(i)}\right) \\ &= \frac{\exp\left(-\frac{1}{2}\left(\mathbf{y}_k - \mathbf{h}_p\left(\check{\mathbf{m}}_k^{(i)}\right)\right)^\top \mathbf{S}_k^{(i)-1}\left(\mathbf{y}_k - \mathbf{h}_p\left(\check{\mathbf{m}}_k^{(i)}\right)\right)\right)}{\sqrt{(2\pi)^{(r+1)}|\mathbf{S}_k^{(i)}|}} \end{aligned} \quad (80)$$

Updated probability of model i :

$$\begin{aligned} \mu_k^{(i)} &= P\left(M_k^{(i)} \mid \mathbf{y}_{1:k}\right) = P\left(M_k^{(i)} \mid \mathbf{y}_k, \mathbf{y}_{1:k-1}\right) \\ &= \frac{P\left(M_k^{(i)} \mid \mathbf{y}_{1:k-1}\right) P\left(\mathbf{y}_k \mid \mathbf{y}_{1:k-1}, M_k^{(i)}\right)}{P\left(\mathbf{y}_k \mid \mathbf{y}_{1:k-1}\right)} \\ &= \frac{P\left(M_k^{(i)} \mid \mathbf{y}_{1:k-1}\right) P\left(\mathbf{y}_k \mid \mathbf{y}_{1:k-1}, M_k^{(i)}\right)}{\sum_{j=0}^r P\left(M_k^{(j)} \mid \mathbf{y}_{1:k-1}\right) P\left(\mathbf{y}_k \mid \mathbf{y}_{1:k-1}, M_k^{(j)}\right)} \\ &= \frac{\check{\mu}_k^{(i)} \Lambda_k^{(i)}}{\sum_{j=0}^r \check{\mu}_k^{(j)} \Lambda_k^{(j)}} \end{aligned} \quad (81)$$

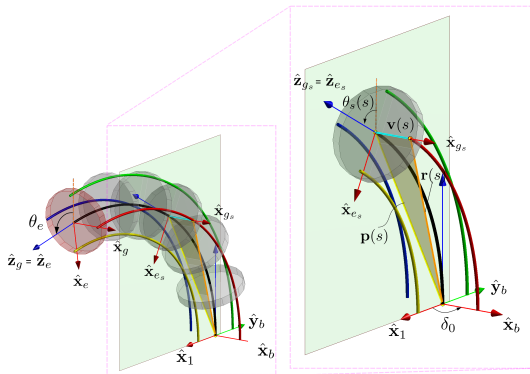


Fig. 16: Schematic of inverse kinematics

REFERENCES

- [1] S. Hirose, "Biologically inspired robots," *Snake-Like Locomotors and Manipulators*, 1993.
- [2] N. Simaan, R. M. Yasin, and L. Wang, "Medical technologies and challenges of robot-assisted minimally invasive intervention and diagnostics," *Annual Review of Control, Robotics, and Autonomous Systems*, vol. 1, pp. 465–490, 2018.
- [3] P. E. Dupont, N. Simaan, H. Choset, and C. Rucker, "Continuum robots for medical interventions," *Proceedings of the IEEE*, vol. 110, no. 7, pp. 847–870, 2022.
- [4] S. Song, Z. Li, H. Yu, and H. Ren, "Electromagnetic positioning for tip tracking and shape sensing of flexible robots," *IEEE Sensors Journal*, vol. 15, no. 8, pp. 4565–4575, 2015.
- [5] P. L. Anderson, A. W. Mahoney, and R. J. Webster, "Continuum reconfigurable parallel robots for surgery: Shape sensing and state estimation with uncertainty," *IEEE robotics and automation letters*, vol. 2, no. 3, pp. 1617–1624, 2017.
- [6] S. Lilge, T. D. Barfoot, and J. Burgner-Kahrs, "Continuum robot state estimation using gaussian process regression on se (3)," *The International Journal of Robotics Research*, vol. 41, no. 13-14, pp. 1099–1120, 2022.

- [7] J. A. Borgstadt, M. R. Zinn, and N. J. Ferrier, "Multi-modal localization algorithm for catheter interventions," in *2015 IEEE international conference on robotics and automation (ICRA)*. IEEE, 2015, pp. 5350–5357.
- [8] A. Ataka, P. Qi, A. Shiva, A. Shafti, H. Wurdemann, H. Liu, and K. Althoefer, "Real-time pose estimation and obstacle avoidance for multi-segment continuum manipulator in dynamic environments," in *2016 IEEE/RSJ International Conference on Intelligent Robots and Systems (IROS)*. IEEE, 2016, pp. 2827–2832.
- [9] C. Shi, X. Luo, P. Qi, T. Li, S. Song, Z. Najdovski, T. Fukuda, and H. Ren, "Shape sensing techniques for continuum robots in minimally invasive surgery: A survey," *IEEE Transactions on Biomedical Engineering*, vol. 64, no. 8, pp. 1665–1678, 2017.
- [10] V. K. Venkiteswaran, J. Sikorski, and S. Misra, "Shape and contact force estimation of continuum manipulators using pseudo rigid body models," *Mechanism and machine theory*, vol. 139, pp. 34–45, 2019.
- [11] J. Y. Loo, K. C. Kong, C. P. Tan, and S. G. Nurzaman, "Non-linear system identification and state estimation in a pneumatic based soft continuum robot," in *2019 IEEE Conference on control technology and applications (CCTA)*. IEEE, 2019, pp. 39–46.
- [12] H. Cheng, H. Xu, H. Shang, X. Wang, H. Liu, and B. Liang, "Orientation to pose: Continuum robots shape reconstruction based on the multi-attitude solving approach," in *2022 International Conference on Robotics and Automation (ICRA)*. IEEE, 2022, pp. 3203–3209.
- [13] R. Peng, Y. Wang, and P. Lu, "A tendon-driven continuum manipulator with robust shape estimation by multiple imus," *IEEE Robotics and Automation Letters*, 2024.
- [14] A. L. Orekhov, E. Z. Ahronovich, and N. Simaan, "Lie group formulation and sensitivity analysis for shape sensing of variable curvature continuum robots with general string encoder routing," *IEEE Transactions on Robotics*, 2023.
- [15] B. Kim, J. Ha, F. C. Park, and P. E. Dupont, "Optimizing curvature sensor placement for fast, accurate shape sensing of continuum robots," in *2014 IEEE international conference on robotics and automation (ICRA)*. IEEE, 2014, pp. 5374–5379.
- [16] Q. Qiao, D. Willems, G. Borghesan, M. Ourak, J. De Schutter, and E. Vander Poorten, "Estimating and localizing external forces applied on flexible instruments by shape sensing," in *2019 19th International Conference on Advanced Robotics (ICAR)*. IEEE, 2019, pp. 227–233.
- [17] Q. Qiao, G. Borghesan, J. De Schutter, and E. Vander Poorten, "Force from shape—estimating the location and magnitude of the external force on flexible instruments," *IEEE Transactions on Robotics*, vol. 37, no. 5, pp. 1826–1833, 2021.
- [18] O. Al-Ahmad, M. Ourak, J. Vlekken, and E. Vander Poorten, "Fbg-based estimation of external forces along flexible instrument bodies," *Frontiers in Robotics and AI*, vol. 8, p. 718033, 2021.
- [19] S. Sefati, M. Pozin, F. Alambeigi, I. Iordachita, R. H. Taylor, and M. Armand, "A highly sensitive fiber bragg grating shape sensor for continuum manipulators with large deflections," in *2017 IEEE SENSORS*. IEEE, 2017, pp. 1–3.
- [20] P. Rao, Q. Peyron, S. Lilge, and J. Burgner-Kahrs, "How to model tendon-driven continuum robots and benchmark modelling performance," *Frontiers in Robotics and AI*, vol. 7, p. 630245, 2021.
- [21] W. S. Rone and P. Ben-Tzvi, "Continuum robot dynamics utilizing the principle of virtual power," *IEEE Transactions on Robotics*, vol. 30, no. 1, pp. 275–287, 2013.
- [22] B. A. Jones, R. L. Gray, and K. Turlapati, "Three dimensional statics for continuum robotics," in *2009 IEEE/RSJ International Conference on Intelligent Robots and Systems*. IEEE, 2009, pp. 2659–2664.
- [23] J. Till, V. Aloï, and C. Rucker, "Real-time dynamics of soft and continuum robots based on cosserat rod models," *The International Journal of Robotics Research*, vol. 38, no. 6, pp. 723–746, 2019.
- [24] F. Boyer, V. Lebastard, F. Candelier, and F. Renda, "Dynamics of continuum and soft robots: A strain parameterization based approach," *IEEE Transactions on Robotics*, vol. 37, no. 3, pp. 847–863, 2020.
- [25] F. Renda, F. Boyer, J. Dias, and L. Seneviratne, "Discrete Cosserat Approach for Multisection Soft Manipulator Dynamics," *IEEE Transactions on Robotics*, vol. 34, no. 6, pp. 1518–1533, dec 2018.
- [26] D. C. Rucker and R. J. Webster III, "Statics and dynamics of continuum robots with general tendon routing and external loading," *IEEE Transactions on Robotics*, vol. 27, no. 6, pp. 1033–1044, 2011.
- [27] S. Huang, D. Meng, X. Wang, B. Liang, and W. Lu, "A 3d static modeling method and experimental verification of continuum robots based on pseudo-rigid body theory," in *2019 IEEE/RSJ International Conference on Intelligent Robots and Systems (IROS)*. IEEE, 2019, pp. 4672–4677.
- [28] H.-J. Su, "A Pseudorigid-Body 3R Model for Determining Large Deflection of Cantilever Beams Subject to Tip Loads," *Journal of Mechanisms and Robotics*, vol. 1, no. 2, 01 2009, 021008.
- [29] M. Khoshnam, I. Khalaji, and R. V. Patel, "A robotics-assisted catheter manipulation system for cardiac ablation with real-time force estimation," in *2015 IEEE/RSJ International Conference on Intelligent Robots and Systems (IROS)*. IEEE, 2015, pp. 3202–3207.
- [30] R. J. Roesthuis and S. Misra, "Steering of multisegment continuum manipulators using rigid-link modeling and fbg-based shape sensing," *IEEE transactions on robotics*, vol. 32, no. 2, pp. 372–382, 2016.
- [31] N. Simaan, R. Taylor, and P. Flint, "A dexterous system for laryngeal surgery," in *IEEE International Conference on Robotics and Automation, 2004. Proceedings. ICRA'04. 2004*, vol. 1. IEEE, 2004, pp. 351–357.
- [32] P. Sears and P. Dupont, "A Steerable Needle Technology Using Curved Concentric Tubes," in *2006 IEEE/RSJ International Conference on Intelligent Robots and Systems*. Beijing, China: IEEE, oct 2006, pp. 2850–2856.
- [33] D. B. Camarillo, C. F. Milne, C. R. Carlson, M. R. Zinn, and J. K. Salisbury, "Mechanics modeling of tendon-driven continuum manipulators," *IEEE transactions on robotics*, vol. 24, no. 6, pp. 1262–1273, 2008.
- [34] R. J. Webster III and B. A. Jones, "Design and kinematic modeling of constant curvature continuum robots: A review," *The International Journal of Robotics Research*, vol. 29, no. 13, pp. 1661–1683, 2010.
- [35] M. W. Hannan and I. D. Walker, "Kinematics and the implementation of an elephant's trunk manipulator and other continuum style robots," *Journal of robotic systems*, vol. 20, no. 2, pp. 45–63, 2003.
- [36] "A Modular Open-Source Continuum Manipulator for Underwater Remotely Operated Vehicles," vol. 14, no. 6, pp. 1–10, dec 2022.
- [37] Q. Zhao, G. Zhang, H. Jafarnejadsani, and L. Wang, "A modular continuum manipulator for aerial manipulation and perching," *arXiv preprint arXiv:2206.06246*, 2022.
- [38] G. S. Chirikjian and J. W. Burdick, "A modal approach to hyper-redundant manipulator kinematics," *IEEE Transactions on Robotics and Automation*, vol. 10, no. 3, pp. 343–354, 1994.
- [39] L. Wang and N. Simaan, "Geometric calibration of continuum robots: Joint space and equilibrium shape deviations," *IEEE Transactions on Robotics*, vol. 35, no. 2, pp. 387–402, 2019.
- [40] P. Rao, Q. Peyron, and J. Burgner-Kahrs, "Shape representation and modeling of tendon-driven continuum robots using euler arc splines," *IEEE Robotics and Automation Letters*, vol. 7, no. 3, pp. 8114–8121, 2022.
- [41] C. D. Santina and D. Rus, "Control oriented modeling of soft robots: The polynomial curvature case," *IEEE Robotics and Automation Letters*, vol. 5, no. 2, pp. 290–298, 2020.
- [42] J. M. Ferguson, D. C. Rucker, and R. J. Webster, "Unified shape and external load state estimation for continuum robots," *IEEE Transactions on Robotics*, 2024.
- [43] Y. Chen, L. Zeng, X. Zhu, K. Xu *et al.*, "Model-based estimation of the gravity-loaded shape and scene depth for a slim 3-actuator continuum robot with monocular visual feedback," in *2019 International Conference on Robotics and Automation (ICRA)*. IEEE, 2019, pp. 4416–4421.
- [44] T. Yuan, Y. Bar-Shalom, P. Willett, E. Mozeson, S. Pollak, and D. Hardiman, "A multiple imm estimation approach with unbiased mixing for thrusting projectiles," *IEEE Transactions on Aerospace and Electronic Systems*, vol. 48, no. 4, pp. 3250–3267, 2012.
- [45] G. Xie, L. Sun, T. Wen, X. Hei, and F. Qian, "Adaptive transition probability matrix-based parallel imm algorithm," *IEEE Transactions on Systems, Man, and Cybernetics: Systems*, vol. 51, no. 5, pp. 2980–2989, 2019.
- [46] I. H. Lee and C. G. Park, "An improved interacting multiple model algorithm with adaptive transition probability matrix based on the situation," *International Journal of Control, Automation and Systems*, vol. 21, no. 10, pp. 3299–3312, 2023.
- [47] R. Hermann and A. Krener, "Nonlinear controllability and observability," *IEEE Transactions on automatic control*, vol. 22, no. 5, pp. 728–740, 1977.
- [48] A. Nahvi and J. M. Hollerbach, "The noise amplification index for optimal pose selection in robot calibration," in *Proceedings of IEEE international conference on robotics and automation*, vol. 1. IEEE, 1996, pp. 647–654.

- [49] S. Macenski, T. Foote, B. Gerkey, C. Lalancette, and W. Woodall, "Robot operating system 2: Design, architecture, and uses in the wild," *Science Robotics*, vol. 7, no. 66, p. eabm6074, 2022. [Online]. Available: <https://www.science.org/doi/abs/10.1126/scirobotics.abm6074>



Guoqing Zhang received the B.E. degree in processing equipment and control engineering from Tianjin University, Tianjin, China, in 2014 and the M.E. degree in Chemical machinery from Xi'an Jiaotong University, Xi'an, China and the M.S. degree in mechanical engineering from Columbia University, New York, NY, USA, in 2019. He is currently a Ph.D. student studying surgical continuum robotics at Stevens Institute of Technology, Hoboken, NJ USA. His research interests include modeling, control, and estimation theory of continuum manipulators and other robotic systems.



Long Wang received the B.S. degree from Tsinghua University, Beijing, China, in 2010, the M.S. degree from Columbia University, New York, NY, USA, in 2012, and the Ph.D. degree from Vanderbilt University, Nashville, TN, USA, in 2019, all in mechanical engineering.

He was a Postdoctoral Researcher with the Department of Mechanical Engineering, Columbia University, New York, NY, from 2018 to 2019. He is currently an Assistant Professor with the Department of Mechanical Engineering, Stevens Institute of Technology, Hoboken, NJ, USA. His research interests include modeling and calibration of continuum robots, surgical robotics, telemanipulation, manipulation, and grasping.